The Astrophysical Journal, 836:35 (18pp), 2017 February 10 https://doi.org/10.3847/1538-4357/836/1/35

OPEN ACCESS

Non-Gaussian Velocity Distributions in Solar Flares from Extreme Ultraviolet Lines: A Possible Diagnostic of Ion Acceleration

Natasha L. S. Jeffrey, Lyndsay Fletcher, and Nicolas Labrosse
School of Physics & Astronomy, University of Glasgow, G12 8QQ, Glasgow, UK
Received 2016 November 2; revised 2017 January 1; accepted 2017 January 5; published 2017 February 7

Abstract

In a solar flare, a large fraction of the magnetic energy released is converted rapidly to the kinetic energy of non-thermal particles and bulk plasma motion. This will likely result in non-equilibrium particle distributions and turbulent plasma conditions. We investigate this by analyzing the profiles of high temperature extreme ultraviolet emission lines from a major flare (SOL2014-03-29T17:44) observed by the *EUV Imaging Spectrometer* (EIS) on *Hinode*. We find that in many locations the line profiles are non-Gaussian, consistent with a kappa distribution of emitting ions with properties that vary in space and time. At the flare footpoints, close to sites of hard X-ray emission from non-thermal electrons, the κ index for the Fe XVI 262.976 Å line at 3 MK takes values of 3–5. In the corona, close to a low-energy HXR source, the Fe XXIII 263.760 Å line at 15 MK shows κ values of typically 4–7. The observed trends in the κ parameter show that we are most likely detecting the properties of the ion population rather than any instrumental effects. We calculate that a non-thermal ion population could exist if locally accelerated on timescales $\leqslant$0.1 s. However, observations of net redshifts in the lines also imply the presence of plasma downflows, which could lead to bulk turbulence, with increased non-Gaussianity in cooler regions. Both interpretations have important implications for theories of solar flare particle acceleration.

Key words: atomic data – line: profiles – Sun: flares – Sun: UV radiation – Sun: X-rays, gamma rays – techniques: spectroscopic

1. Introduction

Solar flare extreme ultraviolet (EUV) spectral line observations with the *Hinode* (Kosugi et al. 2007) *EUV Imaging Spectrometer* (EIS; Culhane et al. 2007) provide information on ion line emissions, plasma temperatures, mass flows, ion abundances, and electron densities (cf. Milligan 2015). For most purposes, Gaussian fitting is an excellent approximation for the low moments of the spectral line—the integrated intensity (zero moment) and line centroid position (first moment)—even if the line profile is non-Gaussian. But the shape of the EUV line profile can be used to infer more about the velocity distribution of the emitting ions. Jeffrey et al. (2016) observed non-Gaussian spectral lines in flare EUV emission, showing that many unblended Fe XVI lines were consistent with a line shape produced by a kappa rather than a Maxwellian velocity distribution, in different flare regions. Megakelvin flare temperatures produce spectral lines dominated by Doppler broadening, and physically, such a line shape could be produced by (1) non-thermal ions of $\lesssim$1 MeV or (2) non-Gaussian turbulent velocity fluctuations, providing a new EUV diagnostic tool.

Non-thermal flare particles are usually detected by X-ray and gamma-ray observations. Most flares have X-ray bremsstrahlung emission from keV electrons, currently detected with the *Ramaty High Energy Solar Spectroscopic Imager* (*RHESSI*; Lin et al. 2002). Only a small minority of (typically) large flares, e.g., SOL2002-07-23 (Krucker et al. 2003), have detectable gamma-ray line emission, produced by interactions between MeV protons and heavier ions (cf. Vilmer et al. 2011), and hence the properties and occurrence of such ions remain uncertain. Accelerated ions with energies less than a few MeV are almost impossible to detect with methods such as impact polarization or charge exchange (e.g., Henoux et al. 1990; Balanca & Feautrier 1998), which also require the presence of anisotropic ion beams, remaining inconclusive. But to assess the non-thermal ion energy content requires knowledge of this accelerated but low-energy component. Ion kappa velocity distributions (cf. Livadiotis & McComas 2009; Pierrard & Lazar 2010) are routinely detected in space physics (see, e.g., Gloeckler & Geiss 1998), but the high density flare environment ($n_e > 10^9$ cm^{-3}) with thermalizing Coulomb collisions is very different from the collisionless solar wind. If such distributions can exist in flare conditions, they could provide a novel diagnostic technique of solar flare ion acceleration unavailable using other methods.

The presence of plasma turbulence might be an alternative explanation for observed solar flare non-Gaussian spectral lines. Excess line broadening, or the presence of broadening larger than expected from isothermal ion motion, is often detected during a flare (e.g., Antonucci & Dodero 1995; Dere & Mason 1993; Doschek et al. 1979, 1980; Alexander 1990; Antonucci et al. 1986), and likely produced by either turbulent magnetic fluctuations (magnetohydrodynamic (MHD) turbulence) or possibly by the superposition of unresolved flows. Although recent EIS studies in active regions and cooler lines in flares showed some correlation between excess line width and directed Doppler shifts (e.g., Milligan 2011), other notable observations, such as larger broadening of hotter lines and isotropy (line broadening is seen for flares located at all heliocentric angles), might be consistent with magnetic fluctuations. Other independent observations using X-ray imaging e.g., by Kontar et al. (2011), also show additional and independent evidence for MHD turbulence in the corona. Further, a recent study (E. P. Kontar et al. 2017, in preparation) shows that MHD turbulence can act as a crucial intermediary in the transfer of large amounts of energy from

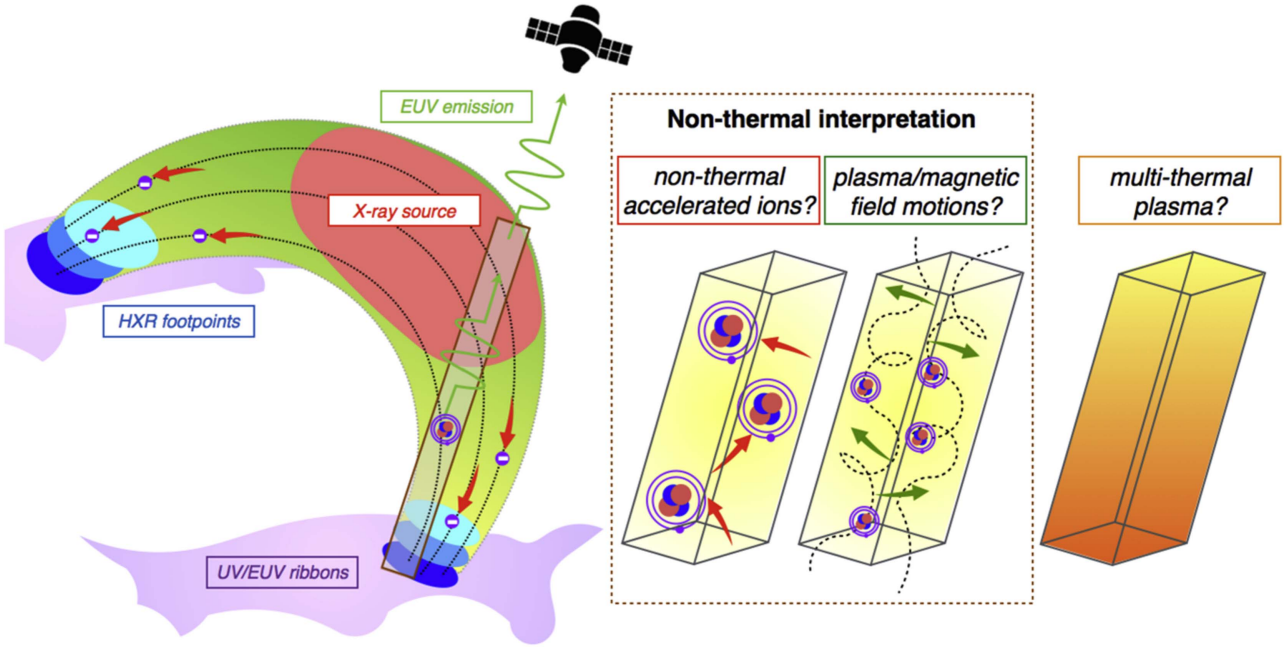

Figure 1. Left: cartoon of the flare and the observations. Right: if an instrumental cause can be eliminated, then the EUV kappa line profiles could be produced by three physical scenarios: (1) a non-thermal ion velocity distribution from isotropic non-thermal ion motions, (2) turbulent motions due to magnetic fluctuations or possibly a superposition of unresolved flows, or (3) a multi-thermal plasma distribution (not discussed in this paper).

stressed magnetic fields to accelerated particles. However, irrespective of the cause, this excess turbulent motion is usually assumed to produce a Gaussian line profile. Indeed, plasma motions in a stochastic turbulent system and described by Brownian motion will produce a velocity probability distribution function (PDF) that is normally distributed. However, large - sporadic motions far exceeding the mean may lead to a velocity PDF with larger and heavier tails than that of a Gaussian, and lead to EUV line profiles better described by a kappa or Lorentzian profile. For example, non-Gaussian magnetic fluctuations are measured in space plasmas (Sorriso-Valvo et al. 1999; Hnat et al. 2002; Pucci et al. 2016), with this intermittency likely to exist on smaller scales in particular. Therefore, any evidence of non-Gaussian line profiles connected to solar flare turbulence could provide an important observational constraint regarding the nature of the turbulence, vital for MHD and kinetic modeling, which is not available via other techniques. Some possible causes of non-Gaussian spectral line profiles, including turbulence and accelerated ions, are shown in Figure 1.

In this paper, we analyze flare SOL2014-03-29T17:44, which shows the presence of non-Gaussian EUV spectral lines. To date, SOL2014-03-29T17:44 is one of the best observed flares in history. As well as observations with *RHESSI* and *Hinode* EIS, the flare was also observed by the *Interface Region Imaging Spectrograph* (*IRIS*; De Pontieu et al. 2014), instruments on board the *Solar Dynamics Observatory* (Pesnell et al. 2012), and the *Dunn Solar Telescope* (*DST*). Hence, it has generated a number of papers studying flare energy (Aschwanden 2015), chromospheric evaporation (Battaglia et al. 2015; Li et al. 2015), multiple wavelength observations and modelling (Heinzel & Kleint 2014; Kleint 2015, 2016; Liu et al. 2015; Young et al. 2015; Kowalski et al. 2016; Rubio da Costa et al. 2016), spectropolarimetric data (Judge et al. 2015), sunquakes (Judge et al. 2014; Matthews et al. 2015), Moreton waves (Francile et al. 2016), and soft X-ray pulsations (Simões et al. 2015). Here, we show that many Fe XVI and Fe XXIII lines, produced at electron temperatures of ∼3 MK and ∼15 MK, respectively, have a line shape consistent with a kappa velocity distribution. We discuss whether the observed non-Gaussian line profiles could be produced by the EIS instrumental profile. We create maps showing the spatial distribution of fitted line properties, such as the κ index and characteristic width, which describe the velocity distribution at each location and time. Finally, we weigh the evidence for the line shapes being due to non-Maxwellian flare-accelerated ions or to non-Gaussian turbulent velocity fluctuations, which would be an observational first.

2. Chosen Flare and Method

SOL2014-03-29T17:44 is an X1.0 flare with coordinates [$X = 510''$, $Y = 265''$]. The X-ray emission starts around 17:44 UT and peaks in soft X-rays (SXRs) at ∼17:48 UT (in the *Geostationary Operational Environmental Satellite* (*GOES*) 1–8 Å). The hard X-ray (HXR, >25 keV) emission peaks around 17:46 UT. The *RHESSI* and *GOES* X-ray light curves of the flare are shown in Figure 2. The start and end times of six EIS rasters covering the rise, peak, and decay times of SOL2014-03-29T17:44 are indicated by gray dotted lines in Figure 2, denoting the time intervals under study. EIS observes SOL2014-03-29T17:44 in fast-rastering mode. Each raster is two minutes and 14 seconds long, with slit movements every ∼12 s. The slit scans in the *X* direction from solar west to east. The $1''$ slit is used during the observations, moving $3.''99$ every slit jump. The natural binning in the *Y* direction is $1''$.

The morphology of SOL2014-03-29T17:44 is shown in Figure 3. The two images in the 304 Å passband of the SDO *Atmospheric Imaging Assembly* (AIA; Lemen et al. 2012) at 17:46:58 UT and 17:49:22 UT show the mainly unsaturated flare ribbons. *RHESSI* X-ray contours at 10–25 keV and at either 25–50 keV or 50–100 keV are overlaid. During raster 17:46:14 UT, two HXR footpoints at 50–100 keV are present, at either side of a lower energy 10–25 keV coronal source. At the later time, the 50–100 keV HXR footpoints disappear but we still observe X-rays up to 50 keV. The EIS intensity

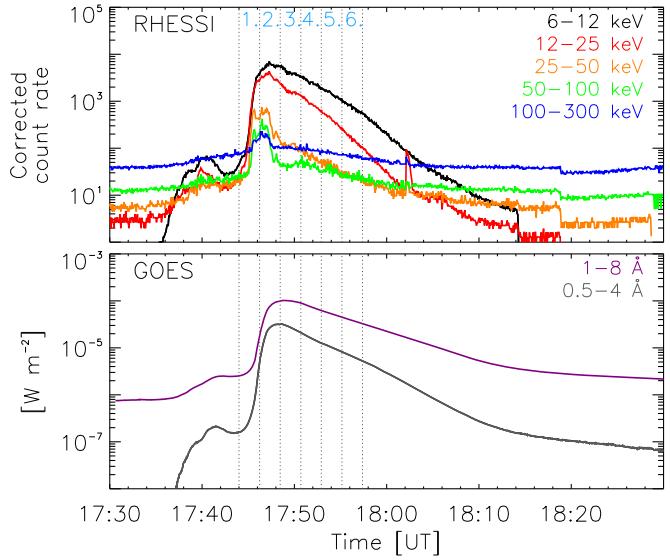

Figure 2. *RHESSI* (top) and *GOES* (bottom) light curves for flare SOL2014-03-29T17:44. The gray dashed lines indicate the start and end times of six EIS rasters covering the flare and the times of study.

contours from the Fe XVI and Fe XXIII EIS rasters are also displayed. The EIS data are aligned with AIA using the procedure eis_aia_offsets.pro, with a 5″ error in *Y*. We assume that AIA and *RHESSI* are well-aligned for the purposes of our analysis.

The EIS data in the *Y* direction is binned into 2″ bins (from 1″), improving the signal-to-noise ratio and line-fitting goodness of fit. The EIS instrumental broadening $W_{\rm inst}$ using the 1″ slit is $W_{\rm inst} = 0.059$ Å (the FWHM) assuming a Gaussian instrumental profile.

2.1. Non-Gaussian Ion and Plasma Velocity Distributions

The EIS data for SOL2014-03-29T17:44 includes two suitably strong, unblended spectral lines formed at different temperatures: Fe XVI (≈2.5–4 MK, $\log T = 6.4$) and Fe XXIII (≈15–16 MK, $\log T = 7.2$). We use the non-Gaussian line profiles to determine the underlying velocity distribution.[1]

For the case of an accelerated ion population and following Bian et al. (2014), a 3D kappa ion velocity distribution $f(v)$ of the first kind can be written as

$$f(v) = \frac{n}{\pi^{3/2} v_{th}^3 \kappa^{3/2}} \frac{\Gamma(\kappa)}{\Gamma(\kappa - 3/2)} \left(1 + \frac{v^2}{\kappa v_{th}^2}\right)^{-\kappa} = A_v \left(1 + \frac{v^2}{\kappa v_{th}^2}\right)^{-\kappa}, \quad (1)$$

where $n = \int f(v) d^3v$ is the number density associated with an accelerated ion distribution and $v_{th} = \sqrt{2k_{\rm B}T/M}$ is a Maxwellian thermal velocity at temperature T (for $k_{\rm B}$ the Boltzmann constant and M the ion mass), and $\Gamma(z) = \int_0^\infty t^{z-1} e^{-t} dt$ is the Gamma function.

To make the link to observed line profiles, we need to convert Equation (1) to a 1D line of sight velocity $v_\parallel$. The 1D ion velocity distribution is given by the integral over all perpendicular velocities $v_\perp$, so that, assuming isotropy,

$$\begin{aligned} f(v_\parallel) &= \int_0^\infty f(v) 2\pi v_\perp dv_\perp \\ &= A_v \int_0^\infty \left(1 + \frac{v_\parallel^2 + v_\perp^2}{\kappa v_{th}^2}\right)^{-\kappa} 2\pi v_\perp dv_\perp \\ &= A_v \frac{\pi \kappa v_{th}^2}{\kappa - 1} \left(1 + \frac{v_\parallel^2}{\kappa v_{th}^2}\right)^{-\kappa+1} \\ \rightarrow f(v_\parallel) &= \frac{n}{\pi^{1/2} \kappa^{1/2} v_{th}} \frac{\Gamma(\kappa - 1)}{\Gamma(\kappa - 3/2)} \left(1 + \frac{v_\parallel^2}{\kappa v_{th}^2}\right)^{-\kappa+1}, \quad (2) \end{aligned}$$

where $n = \int_{-\infty}^{\infty} f(v_\parallel) dv_\parallel$.

As $\kappa \rightarrow \infty$, Equation (2) tends to a 1D isothermal Maxwellian distribution. In this form, we can think of $v_{\rm th}$ as the thermal speed of a Maxwellian ion population before acceleration, or a characteristic speed of the distribution.[2] For low κ and large $v_\parallel$, we can approximate the ion velocity distribution as a power law with $f(v_\parallel) \approx v_\parallel^{-2(\kappa-1)} = v_\parallel^{-\beta}$.

The line of sight velocity distribution is related to the emitted line profile by $f(v_\parallel) \propto I(\lambda) \frac{d\lambda}{dv_\parallel} = I(\lambda) \frac{\lambda_0}{c}$, for wavelength λ, rest wavelength λ_0 and speed of light c, giving

$$I(\lambda) = A_\lambda \left(1 + \frac{(\lambda - \lambda_0)^2}{\kappa 2\sigma_\kappa^2}\right)^{-\kappa+1}, \quad (3)$$

where $v_{th}^2 = 2k_{\rm B}T/M = 2\sigma_\kappa^2 c^2/\lambda_0^2$ and $A_\lambda \propto A_v c/\lambda_0$. As $\kappa \rightarrow \infty$ in Equation (3), the line shape becomes Gaussian. Also, if $\kappa = 2$, the line profile is the same as a Lorentzian. Hence, a kappa line profile can be used as a general line-fitting form that can cover the specific cases of both Gaussian and Lorentzian line profiles. A kappa distribution might also be used to describe a spectrum of velocities $F(u_\parallel)$ produced by plasma turbulence. In this case, the plasma velocity distribution (excluding the ion thermal motions) could be described by

$$F(u_\parallel) = \frac{F_0}{\kappa^{1/2}} \frac{\Gamma(\kappa - 1)}{\Gamma(\kappa - 3/2)} \left(1 + \frac{(u_\parallel - u_1)^2}{\kappa u_0^2}\right)^{-\kappa+1}, \quad (4)$$

where $u_\parallel$ is the plasma velocity, F_0 is a function dependent on plasma properties, u_0 is a characteristic speed of the turbulence, and u_1 is a bulk flow plasma velocity. The overall velocity distribution would then be a convolution of $F(u_\parallel)$ with the ion velocity distribution, but the overall line profile and its non-Gaussianity could still be approximated by a kappa-line distribution. Hence, regardless of the physical process, a kappa-line profile is an excellent starting point for the detection and analysis of non-Gaussian ion or plasma velocities. Even if the kappa distribution does not describe all the underlying physics, it provides a mathematically convenient line profile for the determination of non-thermal/non-Gaussian velocities from *Hinode* EIS data (where more detailed fitting is not possible), providing a fitting function that can range from a Gaussian to a Lorentzian.

[1] It is also possible that a multi-thermal plasma along the line of sight could be responsible, particularly if the ions and electrons have different temperature distributions, but this is not discussed here.

[2] Equation (2) is slightly different from the kappa function used in Jeffrey et al. (2016), where the index $(-\kappa)$ was used instead of $(-\kappa + 1)$.

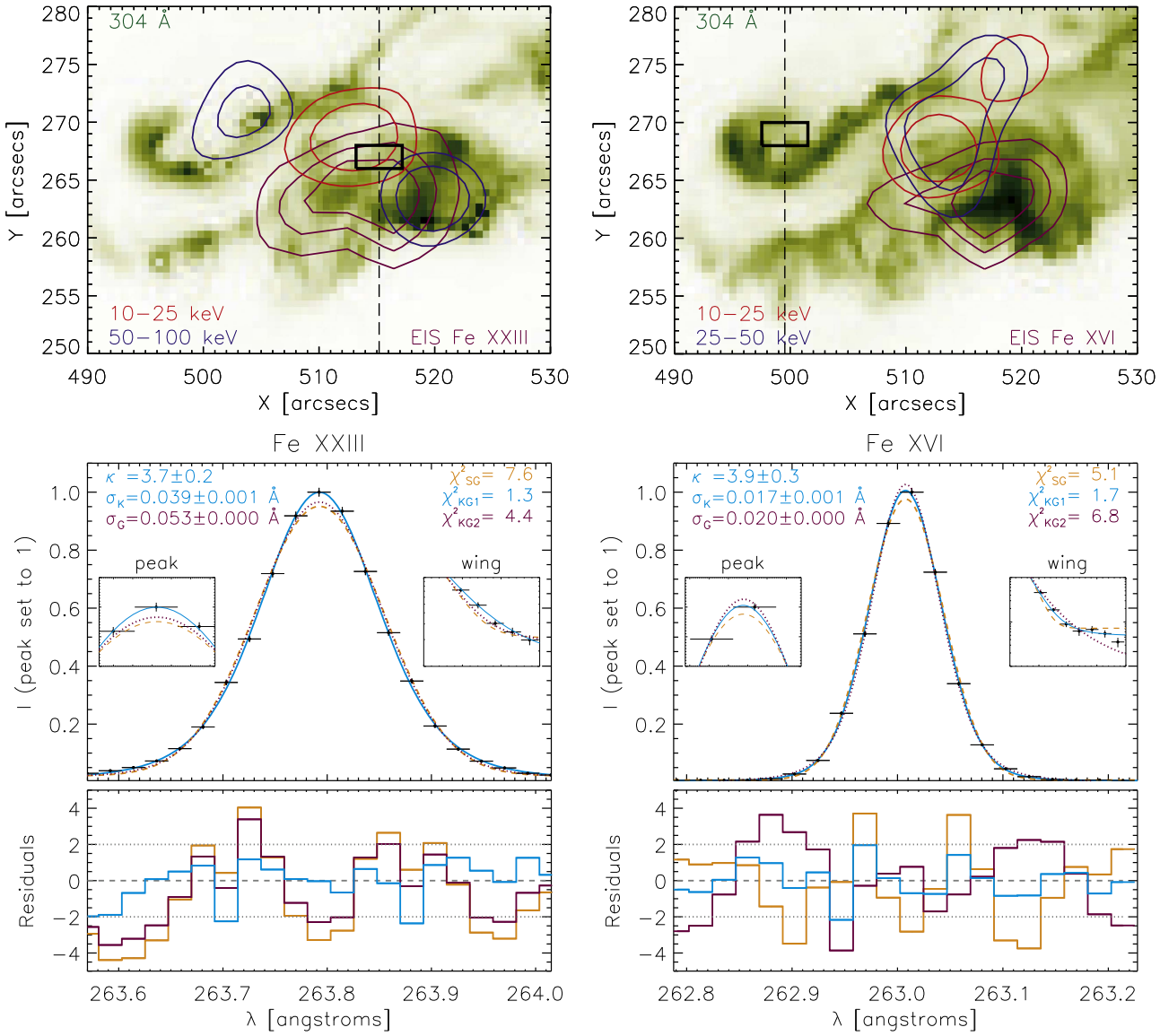

Figure 3. Top row: two SDO AIA images of SOL2014-03-29T17:44 using the 304 Å passband (green background image) at 17:46:59 UT (left) and 17:49:22 UT (right), times within two different EIS rasters. *RHESSI* contours at 10–25 keV (red) and at either 25–50 keV or 50–100 keV (navy blue) are displayed at levels of 50% and 70% of the maximum. Fe XXIII (left) and Fe XVI (right) intensity contours are displayed in purple, at 30%, 50%, and 70% of the maximum. Bottom row: spectral lines of either Fe XXIII (left) or Fe XVI (right) observed at the location of the rectangular box shown in the top images. Each line is fitted with the KG1, KG2, and SG fits (see the text for details). The small panels display the line peak and right wings in detail so that the fits can be clearly seen. The reduced χ^2, residuals, and fit parameters of κ and σ are also displayed.

2.2. EIS Line Fitting of Fe XVI and Fe XXIII

The Fe XVI and Fe XXIII lines are fitted with a single Gaussian to estimate the Gaussian intensity, centroid, and line width. Lines with skewness $|S| > 0.08$, indicating lack of symmetry and probable moving components, are removed from the study. Many of the Fe XVI and Fe XXIII lines fitted with a Gaussian have high reduced χ^2 values, greater than 6. From the Gaussian fitting, even after the removal of a Gaussian instrumental profile with FWHM $W_{\rm inst} = 0.059$ Å, the Doppler broadening in most regions is larger than expected from an isothermal plasma. The Gaussian line widths after the removal of $W_{\rm inst}$ for Fe XXIII can be as large as 0.12 Å and for Fe XVI as large as 0.08 Å. The expected isothermal widths for Fe XXIII and Fe XVI are $W_{\rm th} \sim 0.1$ Å (for $\log T = 7.2$) and $W_{\rm th} \sim 0.04$ Å (for $\log T = 6.4$).

Next, as in Jeffrey et al. (2016), we re-fit the lines with a convolved kappa–Gaussian distribution, accounting for (1) a Gaussian EIS instrumental profile with $W_{\rm inst} = 0.059$ Å and (2) the possibility of a non-Maxwellian velocity distribution resulting in line profiles with higher peaks and "heavier" wings than a Gaussian. The convolved kappa ($\mathcal{K}$)–Gaussian ($\mathcal{G}$) line profile is given by

$$\mathcal{W}(\lambda) = \mathcal{G}(\lambda) * \mathcal{K}(\lambda) = A[0] + A[1] \times \sum_{\lambda'} \exp\left(-\frac{(\lambda' - A[2])^2}{2\sigma_I^2}\right) \times \left(1 + \frac{(\lambda - \lambda' - A[2])^2}{2A[3]^2 A[4]}\right)^{-A[4]+1}, \quad (5)$$

where there are five free fit parameters A. For further details, see Jeffrey et al. (2016). From Equation (5), we are interested in determining the values of the kappa index κ and characteristic width σ_κ (fit parameters $A[4]$ and $A[3]$ respectively), parameters

that provide information about the velocity distribution. We call this fit KG1. As discussed in Jeffrey et al. (2016), this function is a generalized Voigt function, with the traditional Voigt function, a convolution of a Gaussian and a Lorentzian, being the limiting case when $A[4] = \kappa = 2$.

It is possible that all or part of the non-Gaussian line shape results from the instrumental profile. There is no reason for the EIS instrumental profile to be Gaussian, although it may be extremely well-approximated as such. For example, the spectrometer might be expected to have an instrumental response closer to a $\mathrm{sinc}^2\lambda$ function. To account for the possibility of a non-Gaussian instrumental response, we fit another convolved kappa–Gaussian distribution (see Equation (15) in the Appendix), where the kappa part is fixed to represent an instrumental profile with chosen κ_I and σ_I, and the Gaussian parameters are free to vary, representing a physical line profile. The EIS instrumental profile can be approximated by a Gaussian profile with FWHM $W_{\mathrm{inst}} = 0.059$ Å. Therefore, the kappa instrumental profile is constrained by the requirement that κ_I and σ_I produce $W_{\mathrm{inst}} = 0.059$ Å when approximated by a Gaussian. To obtain this we choose $\kappa_I = 3$ and $\sigma_I = 0.0395$ Å. This parameter choice is not unique and the choice of values are discussed further in the Appendix. We call this fit KG2.

The line goodness of fits are judged by a combination of "judgement by eye," a reduced $\chi^2 = \frac{1}{\mathrm{DOF}} \sum_i \frac{(o_i - m_i)^2}{\epsilon_i^2}$ from the weighted least-squares fit, where o_i are the observed intensity values, ϵ_i are the observed intensity error values, m_i are the model values, and degree of freedom DOF = number of data points – number of fitted parameters, and by examining the fit residuals $R = \frac{o-m}{\epsilon}$.

The bottom row of Figure 3 displays two examples: one Fe XVI and one Fe XXIII profile and fit. Here the lines are fitted with (1) a physical kappa–instrumental Gaussian fit (KG1), (2) an instrumental kappa–physical Gaussian fit (KG2), and (3) a single Gaussian (SG). The corresponding spatial locations are indicated in the images shown in the top row of Figure 3 by the rectangular boxes and slit positions (dashed lines). Each image displays the AIA 304 Å passband where two north and south ribbons can be clearly seen. *RHESSI* X-ray contours at 10–25 keV and at either 25–50 keV or 50–100 keV and Fe XVI or Fe XXIII contours are displayed. Figure 3 shows how the kappa part of the KG1 fit is able to account for the higher peaks and broader wings of the observed spectral lines. For both profiles in Figure 3, the single Gaussian fits produce the large reduced χ^2 values of $\chi^2_G = 7.6$ (Fe XXIII) and $\chi^2_G = 5.1$ (Fe XVI). The KG1 fits give the lowest reduced χ^2 values of $\chi^2_{KG} = 1.3$ (Fe XXIII) and $\chi^2_{KG} = 1.7$ (Fe XVI). The KG2 fits produce higher reduced χ^2 values than the KG1 fits with $\chi^2_{KG2} = 4.4$ (Fe XXIII) and $\chi^2_{KG2} = 6.8$ (Fe XVI). The lines displayed in Figure 3 are two examples where the KG1 fit (physical kappa profile) gives a lower goodness of fit than the KG2 fit (instrumental kappa profile). The example line fits in Figure 3 support a physical rather than an instrumental origin since the lines are best fitted with different kappa parameters, and not the single fixed κ_I and σ_I values of the constraint, as we might expect if the non-Gaussian part of the profile was wholly instrumental. We discuss this in greater detail in the Appendix and later in Section 3.2.

In Figure 3, the residuals for each spectral line are also shown. For the chosen Fe XXIII line, the residuals clearly show that the KG1 model is a better fit for the line, as indicated by the low χ^2_{KG1} value. This is particularly noticeable around the peak and the wings of the line, where the KG1 residuals are very close to zero (values within ±2), compared to the fixed KG2 and SG residuals (values within ±4). Again, for the chosen Fe XVI line, the KG1 residuals show that this model is a better description of the line than a Gaussian (SG), for all wavelengths covering the line profile (again the KG1 residual values are within ±2).

We perform two line profile studies. The initial study fits, with the KG1, KG2, and SG functions, lines that satisfy the following two criteria:

1. Lines must have an absolute value of skewness less than 0.08 (to remove lines with moving components as discussed; also see Jeffrey et al. 2016).
2. The estimated noise level (calculated as the standard deviation of the ratio of the intensity errors to intensity for each line) for the line must be below 9% and the ratio of the integrated intensity error to integrated intensity less than 0.9%.

Following the line fitting with the KG1, KG2, and SG profiles, we identify those fits where we are confident that KG1 is the best fit, according to the following extra criteria:

3. The reduced χ^2 values of the kappa–Gaussian fits must be less than 5.0.
4. The reduced χ^2 values of the Gaussian fits must be greater than 3.0.
5. The ratio χ^2_G/χ^2_{KG} must be greater than 2.0 (for both KG1 and KG2).

Criterion 2 is used as a "noise value", which we define as 100% × STD(ϵ/o) (for STD = standard deviation). From the work in Jeffrey et al. (2016) and by testing model lines with different levels of Gaussian noise, we found that lines with a noise value less than ∼10% were usually suitable (i.e., small intensity error values) for a line model comparison. The integrated intensity error to integrated intensity ratio of 0.9% was chosen by trial and error and by examining how this value changed for lines found to be either suitable or unsuitable for study. Criterion 2 allows us to quickly remove a large fraction of unsuitable lines in each raster without examining each line in detail, since each map has a total of ∼660 lines. Further, criteria 3–5 help non-Gaussian line shapes to be found and lines with larger errors that can be well-fitted by all models (i.e., all that produce low χ^2 values) to be removed, helping to pinpoint and only examine lines that have a definite non-Gaussian shape. In particular, criteria 4 and 5 are used to remove lines where the Gaussian model has low $\chi^2 < 3$ since we want to look at (a) non-Gaussian lines and (b) remove noisy lines well-fitted by any model.

None of the Fe XVI regions contained warm pixels (as discussed in Jeffrey et al. 2016), but four Fe XXIII regions did contain warm pixels. In the initial analysis of Section 3, warm pixels are included but they are removed in further analysis of KG1. We also varied the EIS line intensities using the codes of Klimchuk et al. (2016) that account for finite binning in wavelength before the lines are fitted.

3. Results

3.1. Initial Comparison of the KG1, KG2, and SG Fits

In Figures 4 and 5, maps of the line-fit parameters κ and $W = 2\sqrt{2\ln 2} \times \sigma_\kappa$, and the goodness-of-fit χ^2 are displayed.

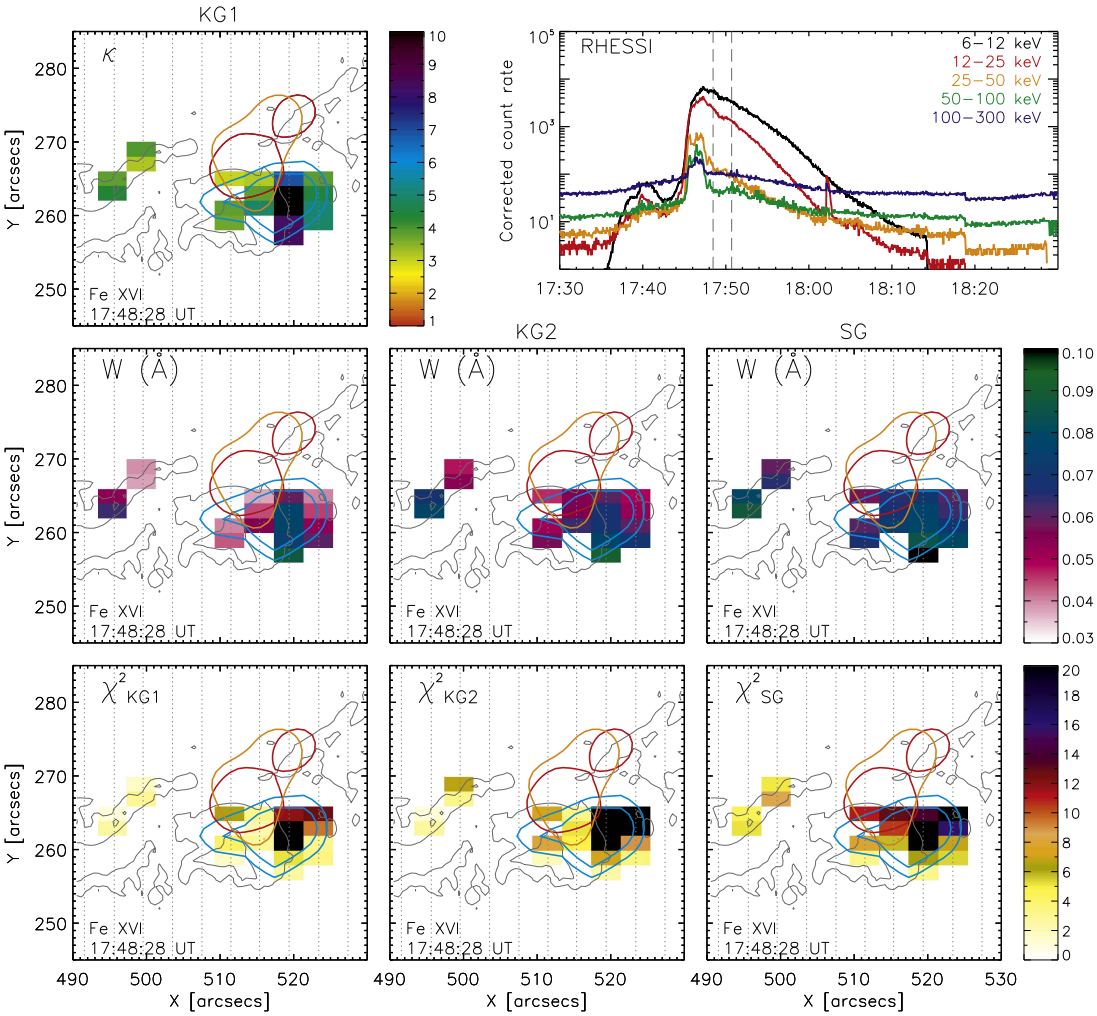

Figure 4. Gaussian (SG) and kappa–Gaussian (KG1 and KG2) fits for Fe XVI. Left column: kappa–Gaussian fit using a Gaussian instrumental profile (KG1), middle column: kappa–Gaussian fit using a kappa instrumental profile (KG2), and right column: single Gaussian fit (SG). Row 1: κ index, row 2: $2\sqrt{2\ln 2}\ \times\ \sigma$ of each fit (σ_κ or σ_G), and row 3: reduced χ^2 values for each fit. The *RHESSI* light curves are also displayed, with gray dashed lines showing the time of observation (time t_3). The parameters from lines shown in this figure satisfy criteria (1) and (2) only (initial study, see text for details).

These are shown for a single EIS raster time of 17:48:23 UT (start time, t_3) and for each of the three fits, KG1 (first column, three panels), KG2 (second column, two panels), and SG (third column, two panels), for Fe XVI (Figure 4) and Fe XXIII (Figure 5). Line widths W are displayed as a "Gaussian FWHM" for easy comparison with line widths found from Gaussian line fitting. At this time, fits satisfying criteria 1 and 2 are located approximately within the Fe XVI 30% intensity contour and along the northern ribbon, and for Fe XXIII, they are mainly within the Fe XXIII 30% contour and close to the 10–20 keV and 25–50 keV X-ray contours.

For the Fe XVI KG1 fit, the lowest values of χ^2_{KG1} (<3) are located at the edges of the Fe XVI source and along the northern ribbon. Closer inspection of the actual line fitting for all fits shows that the high χ^2_{KG1} (∼10) values close to the center of the Fe XVI source are due to the line having a moving component not removed by the skewness condition (the shape of some line profiles with a large moving component can lead to the line shape having a lower skewness than 0.08). The KG1 W values in regions of low χ^2_{KG1} are between 0.04 Å and 0.07 Å. For the KG2 fit, the χ^2_{KG2} values are low in a number of locations, but with higher values than the KG1 fit. The κ index and σ_κ values for the KG2 fit are kept constant at 3 and 0.0395 Å, respectively, and the KG2 Gaussian widths ($2\sqrt{2\ln 2}\ \times\ \sigma_G$) are found to be >0.05 Å. The SG χ^2_{SG} values are higher (often greater than 3) and the SG widths are >0.06 Å. For the Fe XXIII KG1 fit, the majority of χ^2_{KG1} values are again very low (mainly <3), apart from two points that have very high χ^2_{KG1} values (greater than 16). Again, on closer inspection, these lines appear to include blueshifted moving components (for all fits). For KG1, the κ index values are found to be between 4 and 10 and W between ∼0.08 Å and 0.10 Å. For KG2, the W values are greater than ∼0.10 Å but the χ^2_{KG2} values are low (⩽4). The χ^2_{SG} for the Fe XXIII SG fits are again higher, just as for the Fe XVI fits, with values above 6. The uncertainties associated with σ inferred from each of the KG1, KG2, and SG fits are small, of the order 10^{-3} Å or less. The errors for the KG1 κ values are of the order 10^{-1} for both Fe XVI and Fe XXIII. The initial analysis and Figures 4 and 5 show three main results:

1. Spatial patterns for the κ index and characteristic width σ_κ (KG1) emerge and these are discussed further in Section 3.3.

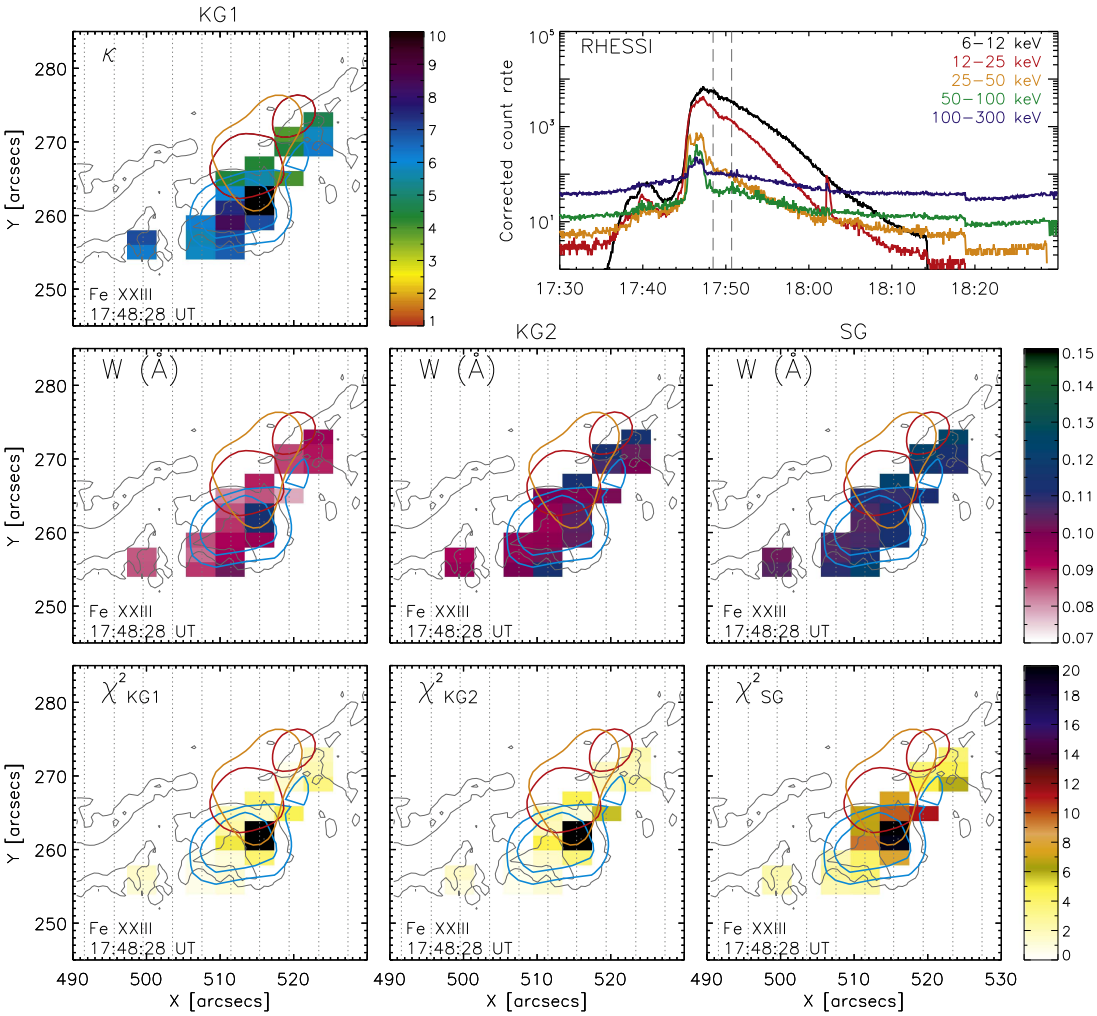

Figure 5. Gaussian (SG) and kappa–Gaussian (KG1 and KG2) fits for Fe XXIII. Left column: kappa–Gaussian fit using a Gaussian instrumental profile (KG1), middle column: kappa–Gaussian fit using a kappa instrumental profile (KG2), and right column: single Gaussian fit (SG). Row 1: κ index, row 2: $2\sqrt{2\ln 2}\times\sigma$ of each fit (σ_κ or σ_G), and row 3: reduced χ^2 values for each fit. The *RHESSI* light curves are also displayed, with gray dashed lines showing the time of observation (time t_3). The parameters from lines shown in this figure satisfy criteria (1) and (2) only (initial study; see text for details).

2. The KG1 and KG2 W values are smaller than those found from the SG fit, which requires the presence of larger excess line broadening to explain the observed values.
3. Overall, the KG1 χ^2_{KG1} values are smaller than the KG2 and SG values, for both Fe XVI and Fe XXIII (with most reduced χ^2_{KG1} values less than two).

3.2. Further Evidence Against an Instrumental Origin for the Non-Gaussian Property

Before analyzing the KG1 fits in detail, we present evidence that the non-Gaussian component of the line profiles are more consistent with a physical rather than an instrumental cause. Further details are provided in the Appendix. In Figure 6, we plot the KG1 κ values versus the characteristic widths $W = 2\sqrt{2\ln(2)}\,\sigma_\kappa$ to observe if there is a trend between changes in the κ index and W, for both Fe XVI and Fe XXIII lines. Only lines that satisfy all five criteria listed in Section 2 are shown in Figure 6. We look for common trends that might suggest that the kappa line profiles are due to an instrumental process instead of a physical one. Importantly, we compare the observed KG1 values in Figure 6 with Figure 13 in the Appendix. Figure 13 displays the results of two modeled lines closely representing Fe XVI and Fe XXIII. Each modeled line is chosen to have an instrumental response represented by either (1) a $\mathrm{sinc}^2\lambda$ function (as discussed in the Appendix) or (2) a kappa function with the chosen parameters $\kappa_I = 3$ and $\sigma_I = 0.0395$ Å (the same as fitting function KG2). Then, each modeled instrumental response is convolved with a Gaussian line representative of a physical line profile and the line width of this Gaussian is varied between sensible values for both Fe XVI and Fe XXIII (see the Appendix). Each resulting modeled line is fitted with the KG1 fitting function, and the KG1 fitted values of the κ index versus W values are then plotted in Figure 13. Figure 13 shows that as the (physical) Gaussian width of the modeled line increases, so do the resulting KG1 fit values of κ index and W, for all modeled lines. The KG1 parameters found from actual fitting to the observed lines and originally shown in Figure 6 are then re-plotted in Figure 13 for comparison with the model line results (lines only satisfying criteria (1) and (2) in Section 2 are also shown). Both Figures 6 and 13 show that the observed values show a range of different W values for a given κ value (and vice versa), which is not suggested by the model line results. The results for Fe XXIII do not match the expected curves at all, while there is a much better match for Fe XVI, although again

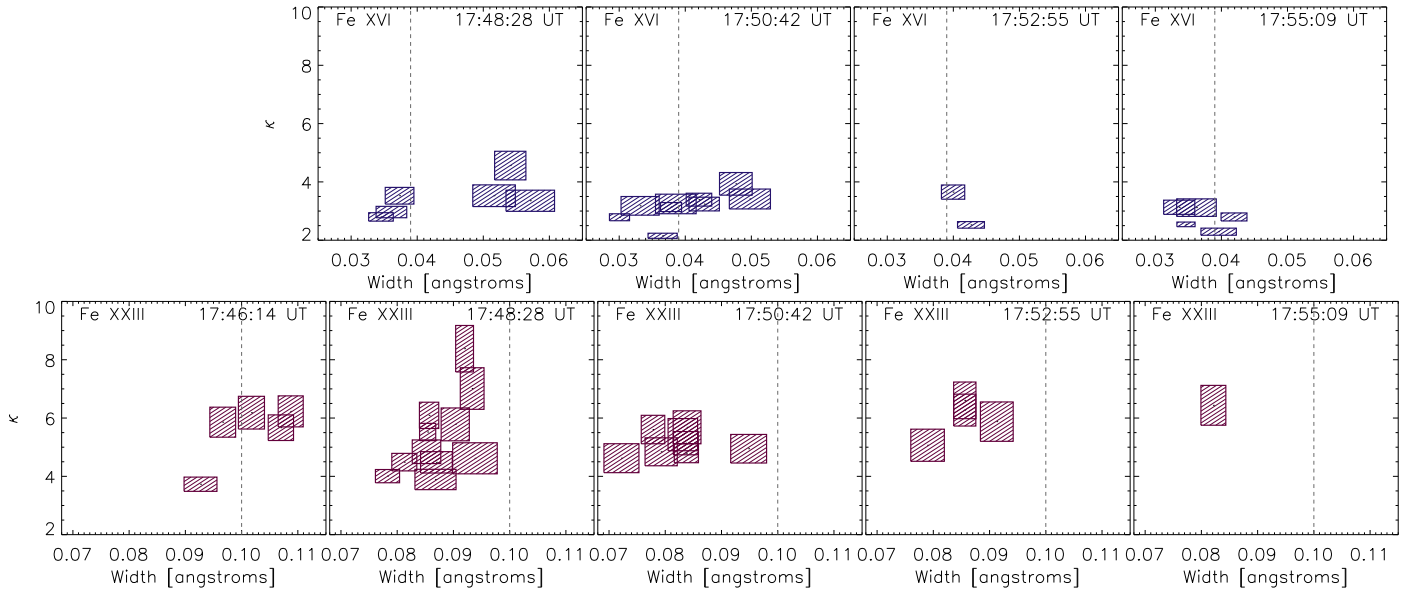

Figure 6. KG1 fit values of κ vs. $W = 2\sqrt{2\ln 2}\ \times\ \sigma_\kappa$ at each time for Fe XVI (top row) and Fe XXIII (bottom row). By plotting κ vs. $2\sqrt{2\ln 2}\ \times\ \sigma_\kappa$ we look for trends that might indicate that non-Gaussian line profiles are due to the instrumental response instead of a physical process. This figure is compared with Figure 13 in the Appendix. The multiple values of κ for a given W (and vice versa) is one observation that supports a physical cause.

we see different values of W for a given κ index. Therefore, this test suggests (but is not conclusive) that the observed non-Gaussian line profiles are physical instead of instrumental, and we interpret the KG1 fitting results as such in the next section.[3]

3.3. Further Analysis of the KG1 Lines

In Figure 7, the flare is shown at six different (EIS start) times t_1 = 17:44:00 UT, t_2 = 17:46:14 UT, t_3 = 17:48:28 UT, t_4 = 17:50:42 UT, t_5 = 17:52:55 UT, and t_6 = 17:55:09 UT. Each map shows AIA 304 Å, *RHESSI*, and EIS contours. Maps of the Fe XVI and Fe XXIII KG1 fit parameters, κ and $W = 2\sqrt{2\ln 2}\,\sigma_\kappa$, are displayed for regions that satisfy all of the criteria listed in Section 2 in Figure 7. At times t_1 and t_2, two HXR footpoints (energies $>$ 50 keV) and an X-ray coronal source are present. At times $t_3 - t_6$, the HXR footpoints disappear but the X-ray coronal source can still be observed. At time t_1 there is no Fe XXIII emission suitable for analysis due to low signal-to-noise ratio and high skewness, likewise for Fe XVI at t_1 and t_2. The Fe XVI and Fe XXIII KG1 fitting parameters (κ and W) plus errors and reduced χ^2 values are also shown in Table 1. For comparison, the KG2 and SG W and χ^2 values are also shown for each line. Overall, over 60% of the lines shown in Figure 7 and Table 1 have KG1 $\chi^2_{KG1} \leqslant 2.0$.

3.3.1. Fe XXIII

During the interval starting at t_2 (covering the HXR peak), five Fe XXIII regions satisfy the five criteria in Section 2.2. These cover part of the coronal 10–25 keV X-ray source and lie within the Fe XXIII 50% contour line. We can see that the κ index increases from north to south, with the lowest values of κ close to the center of the coronal X-ray source increasing from $\kappa \sim 3.8$ to $\kappa \sim 6.5$. Similarly, the largest values of W occur closer to the center of the Fe XXIII source, with values ranging from $W = 0.09$ Å to $W = 0.11$ Å. At t_3 the HXR footpoints disappear, and there is an X-ray coronal source located close to $X = 520''$, $Y = 275''$. We fit with KG1 Fe XXIII lines from 11 locations along the southern edge of the coronal X-ray source, finding κ between 4 and 9. The W values are lower than t_2, ranging between $W \sim 0.08$ Å and $W \sim 0.095$ Å. At t_4, there are eight regions suitable for study with κ ranging between 4.5 and 6. W ranges between 0.07 and 0.095 Å, with all values lower than the expected Gaussian thermal width of 0.1 Å. At t_5 and t_6, the Fe XXIII κ values are ≈6–7 with $W \sim$ 0.08–0.095 Å.

3.3.2. Fe XVI

Overall, the κ values found for Fe XVI are smaller than those for Fe XXIII. At time t_3, there are six locations with Fe XVI lines satisfying our criteria. Close to the center of the Fe XVI source and overlapping slightly with the edge of the coronal X-ray source, we find two locations with κ values of 3 and 4. At $X = 495''$, $Y = 265''$, close to the eastern footpoint, the κ values are between 3.5 and 4. Overall, the κ values for Fe XVI are lower than for Fe XXIII at this time. At time t_4 there are nine suitable Fe XVI pixels, with κ between 2.5 and 4. These are scattered, mostly located at the periphery of the main Fe XVI source and at some distance from the coronal X-ray source.

At t_4, t_5 and t_6, the Fe XVI W values are between 0.03 Å and 0.05 Å, slightly lower than the Fe XVI values at t_2, with the majority between 0.05–0.06 Å. Overall, the largest KG1 W values occur at early times for Fe XXIII and Fe XVI.

4. Physical Interpretation and Discussion

Our analysis can be summarized as follows:

1. Non-Gaussian line profiles consistent with kappa distributions of emitting ions were found during the flare, close to the flare loop top, HXR footpoints, and ribbons

[3] Although we have provided evidence of why the non-Gaussian line profiles are more likely to be physical, it is difficult to rule out an instrumental cause completely. Therefore, if we wish to perform more detailed flare spectroscopy studies and use line shape as a reliable diagnostic tool in the future, then the exact instrumental profile must be laboratory tested before launch.

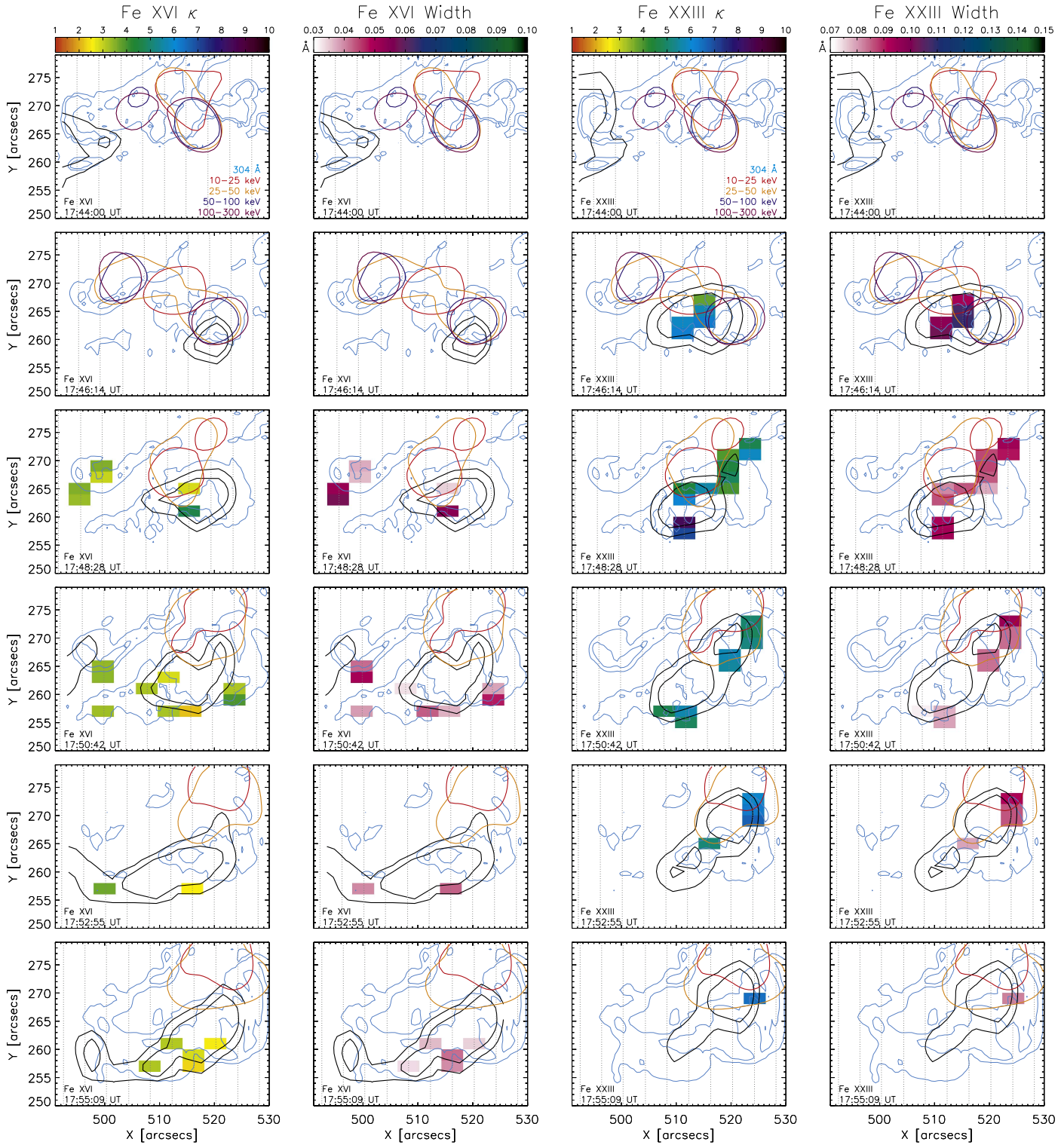

Figure 7. Maps of SOL2014-03-29T17:44 during six different EIS raster times (time $t_1 - t_6$ increases from top to bottom), showing the results of KG1 fits satisfying all five criteria (Section 2). Columns one and two: Fe XVI κ (1) and $W = 2\sqrt{2\ln 2}\ \times \sigma_\kappa$ (2). Columns three and four: Fe XXIII κ (3) and $W = 2\sqrt{2\ln 2}\ \times \sigma_\kappa$ (4). The values are also shown in Table 1.

(similar to SOL2013-05-15T01:45, analyzed in Jeffrey et al. 2016).

2. Fe XVI lines exhibiting kappa profiles were situated farther from the coronal source than the Fe XXIII lines, and often in regions where HXR sources were previously observed.
3. Fe XXIII lines exhibiting kappa profiles were situated close to the coronal source and appeared to move with the coronal source over time.
4. The κ index values of the Fe XVI lines were smaller than those of Fe XXIII and not so systematic in terms of position and value.

Table 1
Fe XVI *(top)* Fe XXIII *(bottom)* KG1 Fitting Parameters (Width W and Kappa Index κ) and Reduced χ^2 Values for all of the Lines Displayed in Figure 7

	KG1			KG2		SG	
	κ	W (Å)	χ^2	W (Å)	χ^2	W (Å)	χ^2
			Fe XVI				
t_3	4.7 ± 0.5	0.054 ± 0.002	2.7	0.070	2.4	0.074	6.1
	3.4 ± 0.4	0.057 ± 0.004	1.2	0.084	2.6	0.088	5.0
	3.5 ± 0.4	0.052 ± 0.003	1.0	0.075	1.7	0.079	4.6
	2.8 ± 0.1	0.035 ± 0.002	3.2	0.061	4.4	0.065	14.6
	3.1 ± 0.2	0.038 ± 0.002	3.3	0.054	3.5	0.065	12.9
	3.9 ± 0.3	0.040 ± 0.002	1.7	0.047	6.8	0.060	5.1
t_4	3.2 ± 0.3	0.039 ± 0.003	1.6	0.060	1.6	0.064	4.7
	3.2 ± 0.2	0.043 ± 0.003	1.1	0.067	1.9	0.070	8.0
	2.2 ± 0.1	0.037 ± 0.002	3.5	0.080	17.7	0.084	27.3
	3.9 ± 0.4	0.048 ± 0.002	1.1	0.067	1.5	0.070	5.0
	3.2 ± 0.3	0.033 ± 0.003	1.8	0.053	1.6	0.058	4.6
	3.1 ± 0.2	0.038 ± 0.002	2.5	0.061	3.0	0.065	15.1
	3.4 ± 0.3	0.050 ± 0.003	1.2	0.074	2.2	0.077	5.2
	2.8 ± 0.2	0.030 ± 0.002	0.7	0.055	1.0	0.059	15.3
	3.4 ± 0.2	0.042 ± 0.002	4.3	0.064	4.4	0.068	12.4
t_5	3.6 ± 0.2	0.034 ± 0.002	0.6	0.058	0.6	0.063	6.0
	2.5 ± 0.1	0.040 ± 0.002	3.5	0.079	13.6	0.083	16.4
t_6	3.1 ± 0.2	0.034 ± 0.002	1.2	0.055	1.0	0.059	5.6
	2.3 ± 0.1	0.040 ± 0.002	1.6	0.080	9.9	0.085	17.5
	2.8 ± 0.1	0.042 ± 0.002	1.8	0.072	6.8	0.077	4.7
	3.1 ± 0.3	0.036 ± 0.003	1.7	0.059	1.6	0.062	5.1
	2.5 ± 0.1	0.035 ± 0.001	4.2	0.067	15.1	0.072	38.7
			Fe XXIII				
t_2	6.2 ± 0.6	0.102 ± 0.002	2.7	0.115	2.8	0.125	5.9
	5.9 ± 0.5	0.097 ± 0.002	2.3	0.110	2.5	0.125	5.8
	6.2 ± 0.5	0.109 ± 0.002	2.9	0.123	3.4	0.120	6.9
	5.7 ± 0.4	0.107 ± 0.002	1.6	0.124	2.8	0.132	6.5
	3.7 ± 0.2	0.092 ± 0.003	1.3	0.125	4.4	0.133	7.6
t_3	7.0 ± 0.7	0.093 ± 0.002	1.4	0.102	1.1	0.112	4.0
	8.4 ± 0.7	0.092 ± 0.002	1.1	0.096	1.6	0.107	4.1
	6.1 ± 0.8	0.086 ± 0.002	2.5	0.096	3.1	0.106	6.9
	4.5 ± 0.4	0.081 ± 0.002	2.0	0.100	2.4	0.110	6.91
	5.5 ± 0.3	0.085 ± 0.002	1.7	0.099	1.3	0.109	10.1
	4.0 ± 0.3	0.078 ± 0.002	4.6	0.100	5.8	0.111	11.4
	4.8 ± 0.4	0.085 ± 0.003	1.9	0.102	2.1	0.112	5.5
	4.5 ± 0.4	0.087 ± 0.003	1.5	0.107	3.2	0.117	5.0
	3.9 ± 0.3	0.087 ± 0.004	0.6	0.113	2.6	0.123	3.8

Table 1
(Continued)

	KG1			KG2		SG	
	κ	W (Å)	χ^2	W (Å)	χ^2	W (Å)	χ^2
	5.8 ± 0.6	0.090 ± 0.003	2.2	0.103	2.9	0.113	4.8
	4.6 ± 0.5	0.094 ± 0.004	1.8	0.115	2.9	0.125	3.8
t_4	4.8 ± 0.5	0.079 ± 0.003	0.9	0.094	1.0	0.105	3.3
	4.6 ± 0.5	0.072 ± 0.003	1.2	0.087	1.2	0.098	3.1
	5.6 ± 0.5	0.078 ± 0.002	2.8	0.088	3.0	0.099	5.7
	5.4 ± 0.6	0.083 ± 0.003	2.1	0.096	2.6	0.106	4.4
	5.7 ± 0.6	0.084 ± 0.002	1.4	0.095	2.0	0.106	3.9
	5.1 ± 0.4	0.084 ± 0.002	3.1	0.098	4.2	0.109	6.9
	4.8 ± 0.3	0.084 ± 0.002	1.5	0.101	1.5	0.111	6.8
	5.0 ± 0.5	0.095 ± 0.003	0.8	0.114	1.4	0.124	3.6
t_5	5.1 ± 0.6	0.079 ± 0.003	1.8	0.093	1.6	0.103	3.6
	6.6 ± 0.6	0.086 ± 0.002	2.4	0.094	2.1	0.104	5.2
	6.3 ± 0.5	0.086 ± 0.002	2.1	0.095	1.8	0.106	5.2
	5.9 ± 0.7	0.091 ± 0.003	1.1	0.104	1.7	0.114	3.0
t_6	6.4 ± 0.7	0.082 ± 0.002	1.4	0.090	1.4	0.100	3.5

Note. For comparison with the KG1 fits shown in Figure 7, the KG2 and SG fitting parameters (width W) and χ^2 are also displayed. The W error values for KG2 and SG are small, all of the order $\sim 10^{-4}$ Å, and are not shown.

5. Fe XXIII showed interesting spatial variations close to the coronal X-ray sources with smaller values of the κ index located closer to the X-ray coronal sources early in the flare.

We considered the possibility that the observed non-Gaussian line profiles result from the EIS instrumental response. Although we cannot rule this out completely, we find that parameter trends for the κ index and σ_κ (particularly for Fe XXIII) do not behave as we would expect if the instrumental response were non-Gaussian. We will now discuss the possible origins of the results.

4.1. The Possible Origin of Non-Gaussian Spectral Lines

Although difficult to detect by other means, it is likely that protons and heavier ions are accelerated during the flare. In Figure 8, we interpret the results as 1D ion velocity distributions $f(v_{||})$ at a single time for Fe XVI (t_3) and Fe XXIII (t_2), obtained using the observed KG1 fit parameters and Equation (2). The 1D distribution is plotted against the |velocity| in km s^{-1} and also as a fraction of the electron thermal speed ($v_{Te} = \sqrt{2k_B T_e/m_e}$ for $\log T_e = 6.4$ (Fe XVI) and $\log T_e = 7.2$ (Fe XXIII)). The gray region denotes ion velocities outside of the maximum fitted ion velocity (from $v_{||} = c\Delta\lambda/\lambda_0$), since the line fits were performed over a range of $\lambda_0 \pm 0.25$ Å (Fe XVI) and $\lambda_0 \pm 0.30$ Å (Fe XXIII), where λ_0 is the line centroid position. The maximum fitted velocities for Fe XVI and Fe XXIII are 250 km s^{-1} and 340 km s^{-1}. The red curve denotes the expected Maxwellian ion velocity distribution at $\log T = 6.4$ and $\log T = 7.2$, while the solid red line denotes the expected ion thermal speed. The expected thermal speeds of Fe XVI and Fe XXIII are ~30 km s^{-1} and ~70 km s^{-1}, respectively. The Fe XXIII results (at t_2, the flare peak) are particularly interesting since we can see the κ index increasing as we move away from the center of the coronal X-ray source towards the center of the Fe XXIII source. This shows that the velocity distribution tends toward Maxwellian farther from the coronal X-ray source. In Figure 9, we compare $f(v_{||})$ versus $|v_{||}|$ for one Fe XVI line and one Fe XXIII line observed in the same spatial region at the same time (t_3). At high velocities, the distribution tends to a power law $f(v_{||}) \sim v_{||}^{-\beta}$ with power index $\beta \approx 2(\kappa - 1)$. The high velocity part of $f(v_{||})$ is fitted with a straight line in log–log space and values of β are shown on the figure legend, with the κ index values. The β values are $\beta = 4.2$ (Fe XVI) and $\beta = 8.9$ (Fe XXIII). Hence, in the same spatial region (but not necessarily the same height), the emitting Fe XVI velocity distribution is farther from Gaussian than the Fe XXIII velocity distribution. This is an interesting result since we might expect the cooler Fe XVI to lie at a lower height in the atmosphere than the hotter Fe XXIII and farther from sites of acceleration, for example. Further, we can estimate (using the fast ion thermalization equations taken from Callen 2006, adapted from Sigmar & Joyce 1971 and Stix 1972) whether the inferred non-thermal ion distributions can exist in a flaring plasma. Kappa distributions are routinely measured in the collisionless solar wind, but the flaring atmosphere is highly collisional with electron number densities of 10^9 cm^{-3} or greater. For fast ions, where $v_{Tf} \ll v \ll v_{Te}$ (for v_{Te} = electron thermal speed and v_{Tf} = heavy ion thermal speed), colliding with a background electron (e)–proton (p) plasma, there are two dominant collisional regimes below and above a velocity v_c given by

$$v_c = \left[\frac{3\sqrt{\pi}}{4}\frac{m_e}{m_p}\right]^{1/3} v_{Te}. \quad (6)$$

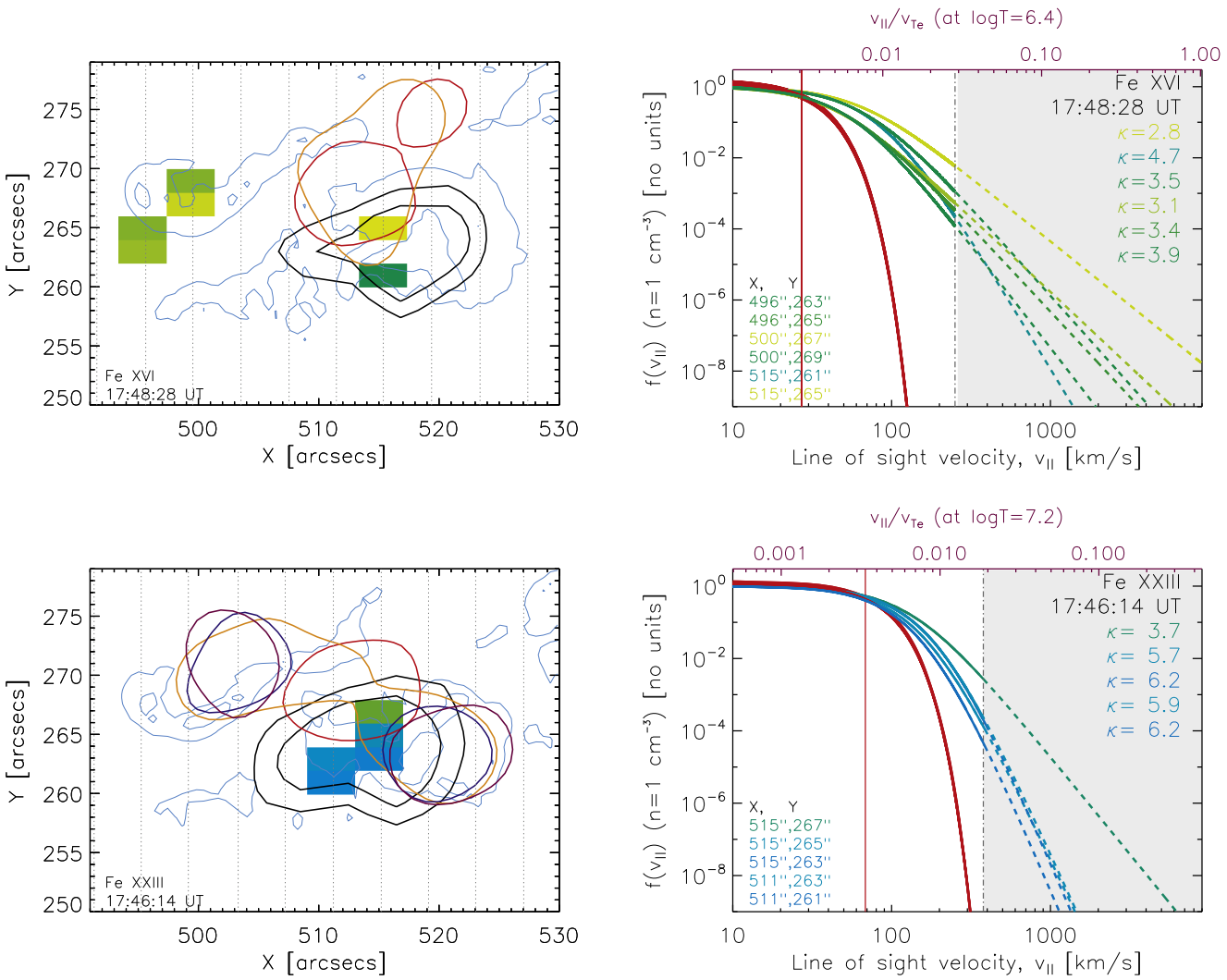

Figure 8. Left: Fe XVI (top) and Fe XXIII (bottom) κ index maps (re-plotted from Figure 7) at two different times (see maps). Right: for each region in the map (left), the forms of the possible ion velocity distributions are determined using Equation (2) and the observed fit values of κ index and σ_κ (corresponding colours). We are only interested in the form of $f(v_{||})$, not the actual values (n is set to 1 and $f(v_{||})$ is also divided by the maximum value for plotting). The red curve denotes the expected Maxwellian velocity distribution with the red vertical line denoting the ion thermal speed. For Fe XXIII, the distribution tends more toward a Maxwellian as the regions move away from the X-ray source (red contour) and toward the center of the Fe XXIII source (black contours). The gray dashed curve indicates the fit cut-off velocity. The errors for $f(v_{||})$ are not shown for clarity (see Figure 9). Error values for κ and W are shown in Table 1. v_{Te} = electron thermal speed at either $\log T = 6.4$ or $\log T = 7.2$.

Here $v_{Te} = \sqrt{2k_B T_e/m_e} = 1.1 \times 10^4$ km s^{-1} and $v_{Tf} = \sqrt{2k_B T_f/m_f} = 34$ km s^{-1} for $T_e = T_p = T_f = 4$ MK (corresponding to Fe XVI). Equation (6) gives $v_c \sim 989$ km s^{-1}. Above v_c, collisions with electrons are dominant but below v_c, collisions with protons are dominant. The maximum velocities determined from the line fitting are only 200–300 km s^{-1}, so only heavy ion–proton collisions are considered.[4]

The Coulomb collisional frequencies (ion–electron f/e and ion–proton f/p) of heavy Fe ions with a background electron–proton plasma are given by

$$\nu_\epsilon^{f/e} \simeq \nu_0^{f/e} \frac{m_f}{m_e} \frac{8}{3\sqrt{\pi}} \left(\frac{v}{v_{Te}}\right)^3 = 2\left(\frac{\epsilon}{\epsilon_c}\right)^{3/2}, \quad (7)$$

$$\nu_\epsilon^{f/p} \simeq \nu_0^{f/e} 2\frac{m_f}{m_p}, \quad (8)$$

where $\epsilon_c = \frac{m_f v_c^2}{2}$ and ν_0 is a reference collisional frequency (or a generalisation of the Lorentz collisional frequency) given-by

$$\nu_0^{f/e}(v) = \frac{n_e \Gamma_{fe}}{v^3} = \frac{4\pi n_e Z_f^2 e^4 \ln\Lambda_{fe}}{m_f^2 v^3}, \quad (9)$$

where Z is the ion charge and assuming the Coulomb logarithm $\ln\Lambda_{fe} = \ln\Lambda_{ee} \sim 20$ in the corona. The heavy ion collisional energy loss rate (total ion energy $\epsilon = m_f v^2/2$, not per nucleon) is then given by

$$\frac{d\epsilon}{dt} = -(\nu_\epsilon^{f/e} + \nu_\epsilon^{f/p})\epsilon, \quad (10)$$

[4] Note that the negligible abundance of heavy ions means that we can ignore heavy ion–heavy ion collisions, compared to the interaction with electrons and protons.

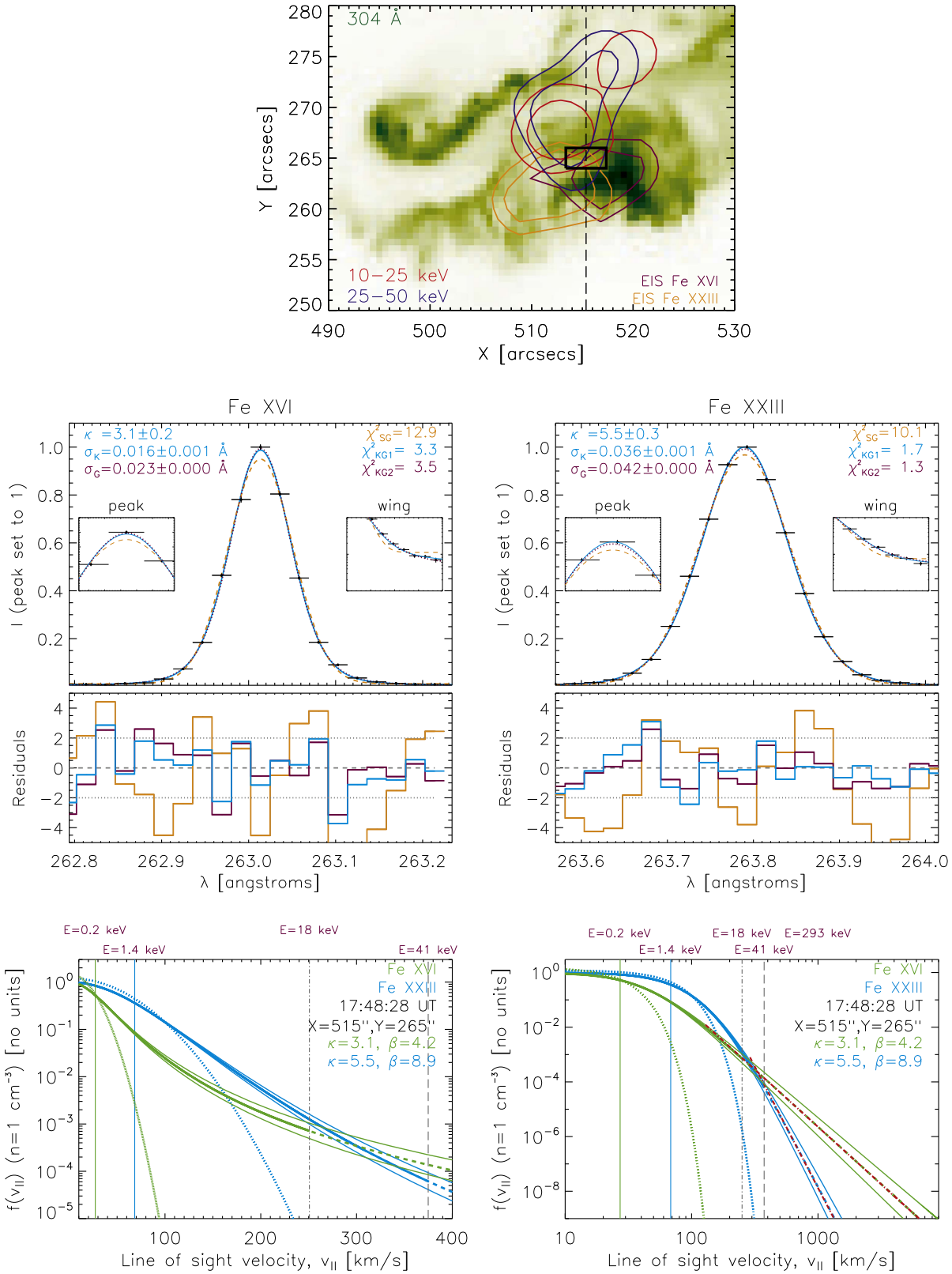

Figure 9. Top: SDO AIA 304 Å image of SOL2014-03-29T17:44 showing *RHESSI* and EIS contours (see legend) and one region (at t_3 (17:48:28 UT) centered at [X $\sim$ 515″, Y $\sim$ 265″]), where line profiles of Fe XXIII and Fe XVI can be fitted by KG1 using the five criteria of Section 2. Middle row: both lines are fitted with a kappa–Gaussian, and they have different values of the κ index. The residuals and χ^2 values show that the kappa–Gaussian fits are a better model than the single Gaussian fit. Bottom row: the kappa line profiles are converted to 1D velocity distributions $f(v_{||})$ using Equation (2) (and divided by the maximum value of $f(v_{||})$). The bottom left panel displays $f(v_{||})$ over the range of velocities fitted during the observation while the bottom right panel shows $f(v_{||})$ plotted over a larger range of $v_{||}$. At large $v_{||}$, a linear fit to $\log f(v_{||})$ vs. $\log v_{||}$ (red lines) gives the velocity power index β, with values displayed in the legend.

or in terms of ion velocity

$$\frac{dv}{dt} = -\frac{v}{\tau_S}\left[1 + \frac{v_c^3}{v^3}\right], \quad (11)$$

where

$$\tau_S = \frac{2}{\nu_\epsilon^{f/e}} \quad (12)$$

is a characteristic fast ion slowing-down time. Integrating Equation (11) allows an estimation of the ion thermalization time,

$$\tau_f \simeq \frac{\tau_S}{3}\ln\left[1 + \left(\frac{\epsilon}{\epsilon_c}\right)^{3/2}\right] = \frac{\tau_S}{3}\ln\left[1 + \left(\frac{v}{v_c}\right)^3\right]. \quad (13)$$

Figure 10 shows the Fe XVI collisional frequencies (divided by the electron number density), energy loss rates (divided by the electron number density), and ion thermalization times for different number densities. The bottom right panel compares the energy loss rate of Fe XVI and Fe XXIII (using $T_e = T_p = T_f = 15$ MK). We can see that the energy loss rate of Fe XXIII at all energies is approximately twice that for Fe XVI. This might explain the higher observed Fe XXIII κ index values. For a number density $n_e = n_p = 10^{10}$ cm^{-3} and an ion velocity of 200 km s^{-1}, the ion thermalization time is $\tau_f \sim 0.01$ s.

The κ index can also be thought of as a parameter that describes the competing processes of particle acceleration and thermalization, and as a ratio of the particle acceleration time ($\tau_{\rm acc}$) to the collisional time (τ_c, inverse of the collisional frequency). It can be written as $\kappa = \Gamma_c/2D_0 = \tau_{\rm acc}/2\tau_c$, where Γ_c is a collisional parameter and D_0 is a diffusion coefficient related to the acceleration mechanism. We can then estimate a local acceleration time using $\tau_{\rm acc} = 2 \times \tau_c\kappa$. For Fe XVI, the average κ value is 3 while for Fe XXIII it is 6. Taking an ion velocity of 200 km s^{-1} and electron number density of $n_e = 10^{10}$ cm^{-3} with $n_p = n_e$ gives an acceleration timescale of $\tau_{\rm acc} = 0.1$ s. τ_c and $\tau_{\rm acc}$ are shown for a range of ion energies in Figure 10 (bottom panel).

The collisional drag force on heavy ions has a minimum for ion speeds below v_{Te} (Holman 1995) and a partial runaway could occur, giving a suprathermal tail of ions with velocities below v_{Te}. However, if we convert the estimated ion thermalization times τ_f to thermalization lengths using $L_F = v\tau_f$, then the thermalization of the observed ions will occur over distances $\ll 1''$, for $n_p = 10^{10}$ cm^{-3}. Therefore, if the line profiles are due to accelerated ions, then they must undergo acceleration *locally and continuously* during the flare time of study. We also note that SOL2014-03-29T17:44 had no observable gamma-ray line emission, so there is no evidence for MeV ions.

We can make a rough estimate of the total energy associated with the observed kappa distributions (without separating the "thermal" and "non-thermal" components). The element and ion abundances are taken from the CHIANTI atomic database (Dere et al. 1997; Landi et al. 2013). If we assume that the range of electron number densities $n_e = n_p$ lie between $10^9 - 10^{11}$ cm^{-3}, then we can estimate that the number densities of Fe XVI and Fe XXIII lie between $n_f = 10^3 - 10^5$ cm^{-3}. Using the observed Fe XVI and Fe XXIII κ index values of 3–6 and plugging them into $f(v)$ [cm^{-6} s^3] (Equation (1)), an estimate of the energy density U [ergs cm^{-3}] above $v_{\rm th}$ is found by numerically integrating

$$U = \int_{v_{th}}^{\infty} \frac{1}{2}Mv^2 f(v) d^3v. \quad (14)$$

In order to turn this into a total energy estimate, E, we can multiply this by the EUV emission volume V. From Figure 7, we estimate the Fe XXIII and Fe XVI volumes (we use times t_2 and t_3, respectively, and assume a spherical volume), and we calculate a volume of the order $V = 10^{27}$ cm^3. We can then estimate a total energy above $v_{\rm th}$ associated with a single ion species (Fe XVI or Fe XXIII) using $E = VU$. Finding the values numerically gives $E \sim 10^{22}$–10^{24} ergs. We have not performed a detailed *RHESSI* spectroscopy analysis for this flare as it was not the purpose of the study but in comparison, the energies associated with electrons in large flares are usually of the order 10^{30} ergs.

An alternative scenario for producing non-Gaussian line shapes is that they originate in macroscopic velocity fields due to plasma turbulence. Support for this possibility comes from the fact that all of the observed Fe XVI and Fe XXIII lines are slightly redshifted, indicating small bulk downflows—even in the corona—which could drive turbulence. An estimate using laboratory rest wavelengths for each line gives downflow speeds of $v_{\rm shift} \sim +30$ to $+70$ km s^{-1}, at nearly all times and locations. It is difficult to estimate an absolute rest wavelength since these high temperature flare lines (particularly Fe XXIII) are not present in quiet Sun regions. After trying to determine an absolute wavelength scale for the cooler Fe XVI line ($\log T \sim 6.4$) using a "quiet Sun" region at the top of the raster at different times, we still find redshift values of $v_{\rm shift} \sim +10$ to $+40$ km s^{-1}, with Fe XVI showing larger shifts. Even taking a rather large uncertainty of $\sim$10 km s^{-1} in the inferred rest wavelength, small redshifts are still present. This interpretation of the non-Gaussian line profiles leads to the interesting possibility of a diagnostic for localized turbulence, which could have profound consequences for theories of flare particle acceleration.

5. Summary

In this paper, we show that in many locations in a flare, the Fe XVI and Fe XXIII line profiles observed by *Hinode* EIS are inconsistent with Gaussian spectral line shapes and are better described by emission from a kappa distribution of ion velocities. We find that the line profile analysis of suitable unblended lines such as Fe XVI and Fe XXIII can provide a powerful diagnostic for microscopic (non-equilibrium) or macroscopic (turbulent) ion velocities during a solar flare, which may help constrain fundamental processes related to localized particle acceleration and/or turbulent magnetic or plasma fluctuations or flows. Straightforward estimates of ion collisional timescales suggest that the required accelerated ion distributions, with energies below 1 MeV, can exist, provided that they are accelerated close to where the EUV line emission originates. Also, the acceleration mechanism must have an acceleration time $\tau_{\rm acc} \leqslant 0.1$ s and must operate for the duration of the flare observations. Although not impossible, these are stringent conditions, suggesting that the alternative possibility, line profiles due to non-Gaussian turbulent velocities, is a more plausible physical explanation. This is also supported by the observation of small redshifts at the

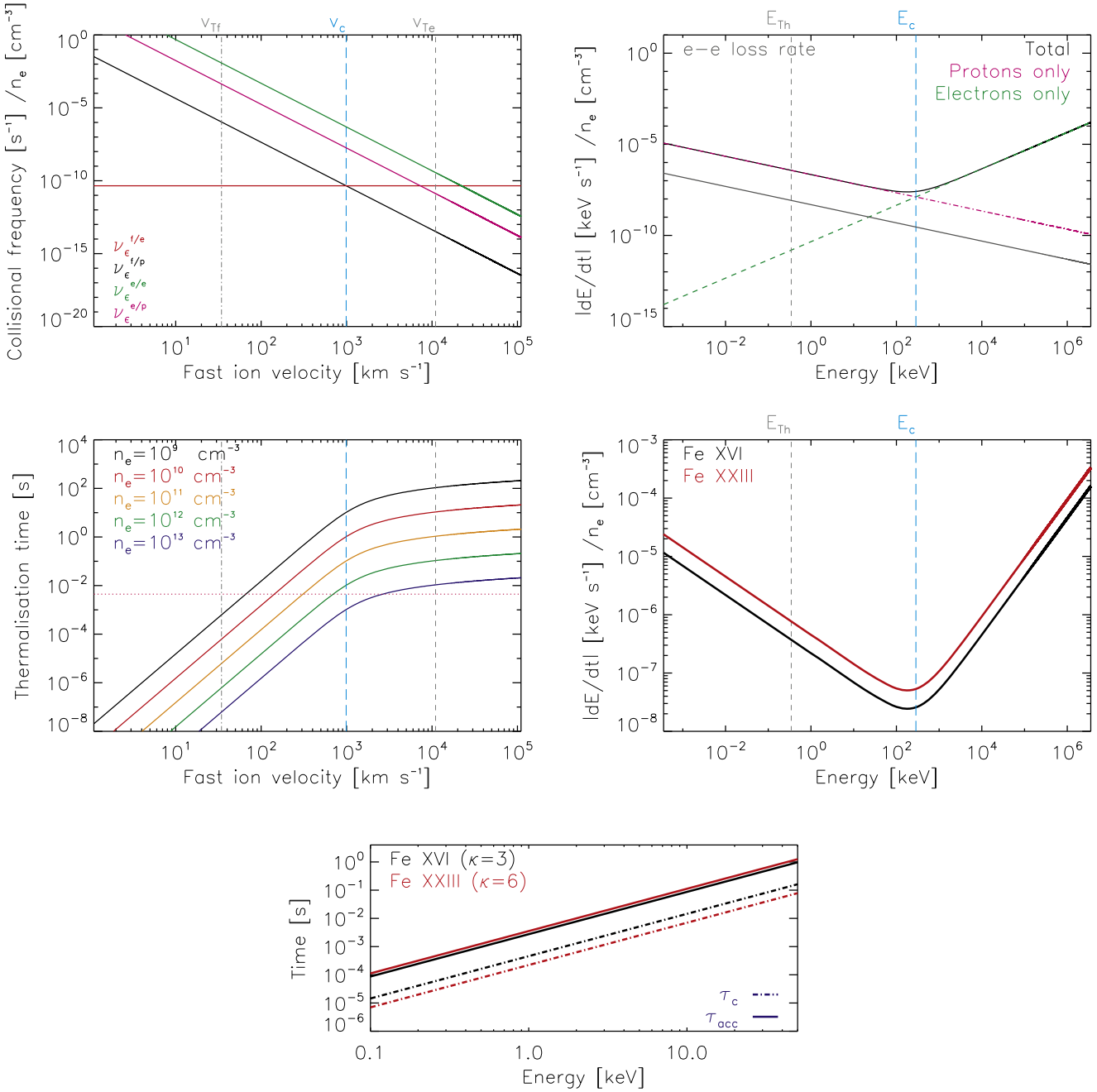

Figure 10. Top left: Fe XVI (f) collisional frequency in an electron (e)–proton (p) background plasma for f–e interactions (red) and f–p interactions (black), vs. ion velocity (km s^{-1}). Top right: energy loss rate dE/dt vs. total ion kinetic energy (not energy per nucleon) for Fe XVI f–e and Fe XVI f–p collisions. The black curve is a combination of both interactions while the f–e (green) and f–p (pink) curves are also shown individually. The energy loss rates for e–e (gray) are also shown for comparison (note these are divided by n_e). At the observed energies of interest, f–p collisions are the dominant interaction. Middle left: the thermalization times for the Fe XVI ions, due to different background electron number densities (where $n_e = n_p$). Middle right: comparison of f–e and f–p energy loss rates for Fe XVI and Fe XXIII. The energy loss rate for Fe XXIII is 2× larger than that for Fe XVI, which might account for the different κ indices observed for both ions. Bottom panel: comparison of the collisional (dashed) and acceleration (solid) times for Fe XVI (black) and Fe XXIII (red) using a number density of 10^{10} cm^{-3}.

sites of non-Gaussian Fe XVI and Fe XXIII profiles. If broadening is due to turbulence, the physical line profile is a convolution of two physical velocities: the ion thermal velocity and a non-Gaussian spectrum of plasma velocities. Further, since SOL2014-03-29T17:44 is the second flare observed with non-Gaussian line profiles, its disk location in comparison to the close-to-limb location of SOL2013-05-15T01:45, studied in Jeffrey et al. (2016), is suggestive of near isotropy more consistent with turbulent magnetic fluctuations rather than unresolved plasma flows. Lastly, it is interesting to note that in many studies of excess broadening, the highest excess broadening occurs for lines formed at the highest temperatures. In this line profile study, we find that although $v_{\rm th}$ is generally higher at early times and for hotter Fe XXIII (for all fits), the least Gaussian profiles (i.e., the smallest κ values) are found for the cooler Fe XVI lines expected to exist at lower heights in the atmosphere.

The line profile analysis used data from *Hinode* EIS with an instrumental broadening of 0.059 Å (1″ slit) and a spectral pixel size of 0.022 Å, and this analysis pushes the limits of

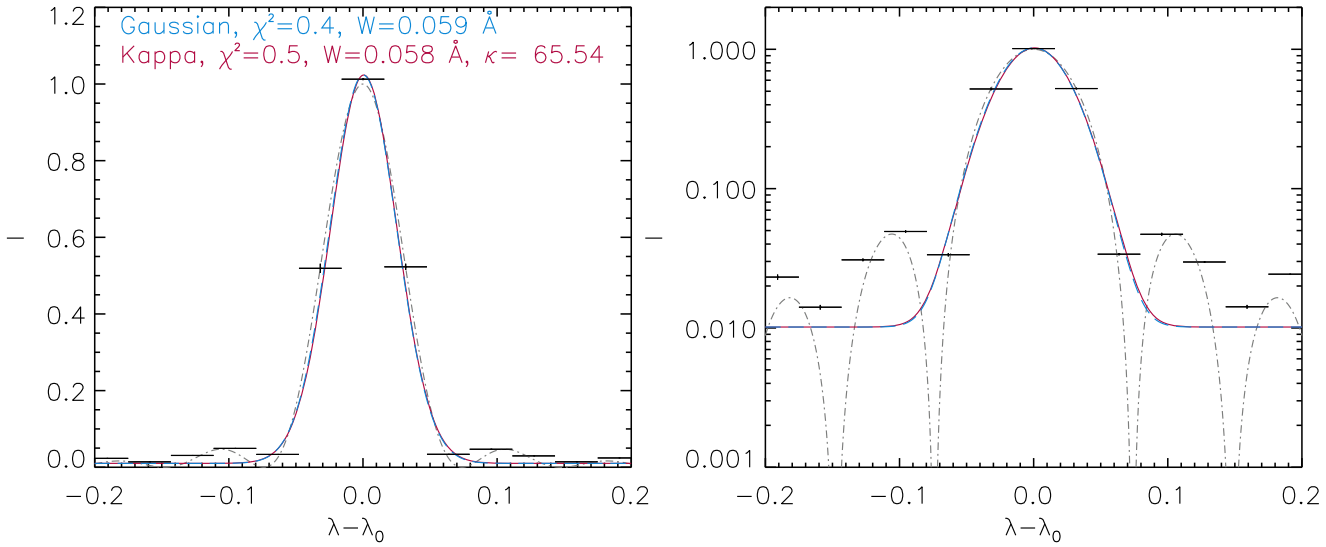

Figure 11. Modeled $\mathrm{sinc}^2\lambda$ line profile using the EIS spectral pixel resolution of 0.022 Å, in a linear Y scale (left) and logarithmic Y scale (right). The same profile with a much higher resolution is displayed using a gray dashed–dotted curve so that the shape of the $\mathrm{sinc}^2\lambda$ line profile can be clearly seen. Both single Gaussian (blue) and single kappa (pink) line profiles are fitted and we can see that the central part of the profiles is well-approximated by a Gaussian distribution (or a kappa distribution tending towards a Gaussian with a κ index ∼66).

EIS. We are as certain as we can be that the non-Gaussian profile is not instrumental; however, it cannot be dismissed completely for EIS. We suggest that the instrumental profile of future EUV spectrometers is measured precisely well into the line wings, so that higher moments of the line shape can be found with confidence from future solar observations.

N.L.S.J., L.F., and N.L. gratefully acknowledge the financial support by the STFC Consolidated Grant ST/L000741/1. CHIANTI is a collaborative project involving George Mason University, the University of Michigan (USA), and the University of Cambridge (UK). *Hinode* is a Japanese mission developed and launched by ISAS/JAXA, collaborating with NAOJ as a domestic partner, and NASA and UKSA as international partners. Scientific operation of the *Hinode* mission is conducted by the *Hinode* science team organized at ISAS/JAXA. This team mainly consists of scientists from institutes in the partner countries. Support for the post-launch operation is provided by JAXA and NAOJ (Japan), UKSA (U.K.), NASA, ESA, and NSC (Norway). The research leading to these results has received funding from the European Community's Seventh Framework Programme (FP7/2007-2013) under grant agreement No. 606862 (F-CHROMA). We thank Dr. David Brooks for providing the original EIS laboratory data and Dr. Eduard Kontar for informative comments.

Appendix
The EIS Instrumental Profile

We test whether the EIS instrumental profile is responsible for the non-Gaussian line shapes observed. We find that many of the observed line profiles are well-fitted (low reduced χ^2 values) using a convolved kappa–Gaussian function, so we fit the same function but in reverse, where the instrumental profile is approximated by a fixed kappa profile and the physical line profile is described using a Gaussian (fit KG2 in the main text). The fitting function $\mathcal{W}_{KG2}$ is then given by

$$\mathcal{W}_{KG2}(\lambda) = \mathcal{G}(\lambda) * \mathcal{K}(\lambda) = A[0] + A[1]\sum_{\lambda'} \times \exp\left(-\frac{(\lambda' - A[2])^2}{2A[3]^2}\right)\left(1 + \frac{(\lambda - \lambda' - A[2])^2}{2\sigma_I^2\kappa_I}\right)^{-\kappa_I+1}, \quad (15)$$

where the instrumental σ_I and κ_I are fixed and the Gaussian $\sigma = A[3]$ represents a physical Gaussian isothermal line width (plus excess broadening). The only constraint for σ_I and κ_I is that the resulting instrumental profile should be approximated by a Gaussian profile with FWHM equal to the instrumental width of $W_{\mathrm{inst}} = 0.059$ Å for the 1″ slit. There is no reason for the instrumental broadening to be kappa in shape but if it is non-Gaussian, the relatively low EIS spectral pixel resolution may produce a profile well-described by such a function. It is possible that the instrumental profile is described by something closer to a $\mathrm{sinc}^2\lambda$ function (Jones et al. 1995), given by

$$I(\lambda) \propto \mathrm{sinc}^2\lambda = \left(\frac{\sin(\alpha\lambda/2)}{\alpha\lambda/2}\right)^2, \quad (16)$$

where α controls the central width of the function. This function is shown in Figure 11. In Equation (16), $\alpha \sim 85$ produces a Gaussian FWHM of $W_{\mathrm{inst}} \sim 0.059$ Å, when fitted with a single Gaussian function.

In Figure 11, we fitted a single kappa function and a single Gaussian function to a $\mathrm{sinc}^2\lambda$ profile with a 5% Gaussian noise level. We find that both the Gaussian and the kappa functions fit the central part of the $\mathrm{sinc}^2\lambda$ function well, with the kappa distribution tending toward a Gaussian with a kappa index larger than 20 (∼66). At the given noise level, the Gaussian and kappa fits gave reduced χ^2 values of 0.4 and 0.5, respectively, but both functions do not fit the higher-order terms.

For further testing, we convolve $\mathrm{sinc}^2\lambda$ with a Gaussian distribution (representing a physical line profile) and fit it with

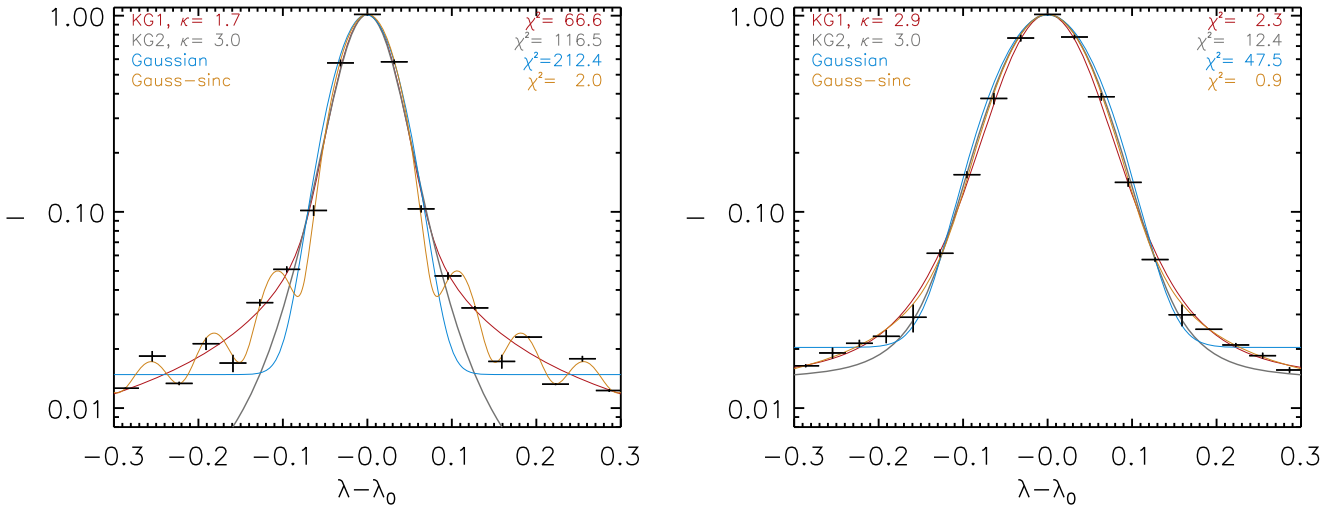

Figure 12. Modeled convolved Gaussian–sinc$^2\lambda$ line profile using the EIS spectral pixel resolution of 0.022 Å for Fe XVI (left) and Fe XXIII (right). The Gaussian part of the profile in the left column represents Fe XVI and the right column Fe XXIII, and each has a noise level of 5%. Each line is fitted with (1) KG1 (pink), (2) KG2 (dark gray), (3) Gaussian (blue), and (4) Gaussian–sinc$^2\lambda$ (orange). The reduced χ^2 values for each fit are also shown.

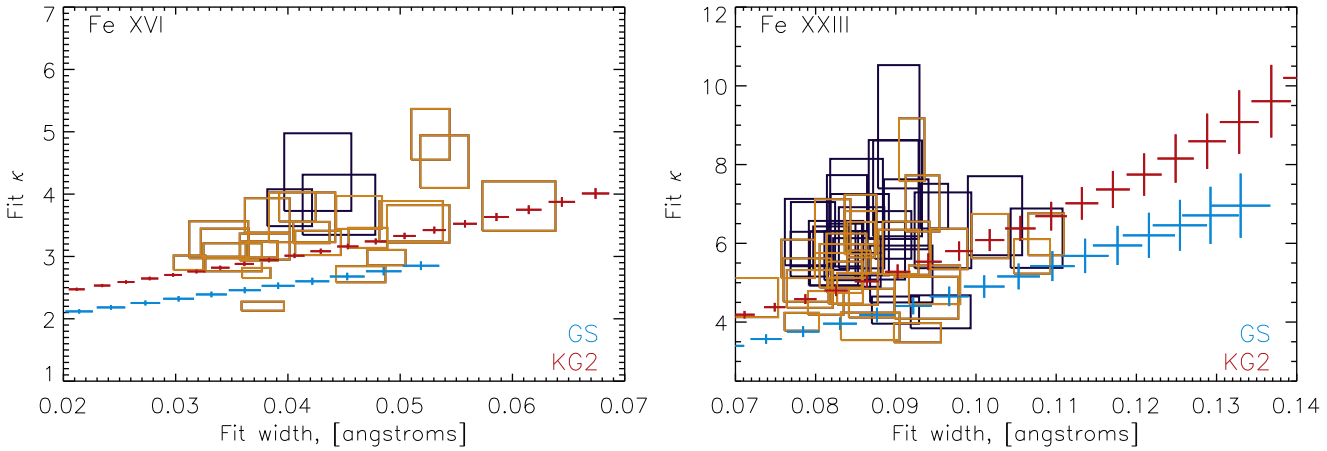

Figure 13. Lines representing Fe XVI and Fe XXIII with Gaussian line widths ranging from 0.039 Å to 0.089 Å and from 0.089 Å to 0.15 Å, respectively, are convolved with either an instrumental profile of the form of (1) a sinc$^2\lambda$ function (as above; blue) or (2) a kappa function with parameters $\kappa_I = 3$ and $\sigma_I = 0.0395$ Å (KG2; red). Again, a 5% noise level is added. The KG1 function is fitted to the lines and the fitted κ index vs. the widths $W = 2\sqrt{2\ln 2}\,\sigma_\kappa$ are shown. The actual observations and fitting results from Section 3 and Figure 6 are also displayed using the orange (using the full criteria as listed in Section 2) and blue (using only criteria 1. and 2. listed in Section 2) rectangles.

a number of different functions: (1) single Gaussian, (2) convolved kappa (physical)–Gaussian (instrumental) (main text KG1), (3) convolved kappa (instrumental)–Gaussian (physical) (main text KG2), and (4) a convolved Gaussian–sinc$^2\lambda$ function. A 5% noise level is again added, and the lines and fits are shown in Figure 12. The physical Gaussian part of the lines represent either Fe XVI with a thermal width $W_{th} = 0.039$ Å or Fe XXIII with $W_{th} = 0.099$ Å. The widths of the Gaussian lines are also increased to represent excess broadening. The κ values found from the KG1 and KG2 fits and the χ^2 values of all fits 1–4 are shown in Figure 12.

For the KG2 fit in the main text, we had to pick instrumental values for the κ_I index and characteristic width σ_I. After iteratively trying values of σ_I and κ_I, $\kappa_I = 3$ was chosen, matching the low κ index values found from the observed Fe XVI line fitting. The value of $\sigma_I = 0.0395$ Å with $\kappa_I = 3$ produces a line profile that can be fitted with a Gaussian to produce a Gaussian FWHM equal to that of an instrumental width $W_{\rm inst} = 0.059$ Å for the the 1″ slit. For the line representing Fe XVI, Figure 12 shows that the Gaussian–sinc^2 function is the best fit ($\chi^2 = 2.1$). This is because the small physical broadening of Fe XVI does not hide the chosen instrumental form. All other functions fit the line profile poorly with high χ^2 values of 66.6 (KG1), 116.5 (KG2), and 212.4 (Gaussian). For the line representative of Fe XXIII, we see that the Gaussian–sinc$^2\lambda$ function is again the best fit ($\chi^2 = 0.9$) since this was the chosen form of the overall line profile. However, in this case, the KG1 fit is able to produce a low $\chi^2 = 2.3$, while KG2 gives $\chi^2 = 12.4$. The χ^2 for the single Gaussian fit is large with a value of 47.5. Overall, the fits here are not representative of our observed EIS line profiles where a single Gaussian function and both the KG1 and KG2 functions tend to fit the line profile with much lower χ^2 values, usually less than 10. For a final test, we vary the Gaussian widths of Fe XVI and Fe XXIII from 0.039 Å to 0.089 Å and from 0.089 Å to 0.15 Å, respectively, and create two examples where the instrumental response is either represented by (1) a sinc$^2\lambda$ function (as above) or (2) a kappa function with parameters $\kappa_I = 3$ and $\sigma_I = 0.0395$ Å (KG2). Again, a 5% noise level is added to the lines. Each modeled line

profile is fitted with a KG1 fit, and we plot the resulting KG1 fitted κ index versus the fitted line width (as Gaussian FWHM). For both lines representing Fe XVI and Fe XXIII, we find that as the physical line width grows so do the KG1 fit parameters of κ and σ_κ. In Figure 13, the results are compared with the observations from Section 3. We can see from Figure 13 that the observed κ indices and $W = 2\sqrt{2\ln 2}\,\sigma_\kappa$ do not follow the trends suggested by the presence of a $\mathrm{sinc}^2\lambda$ or KG2 instrumental response, particularly for Fe XXIII where for a given κ index, W can take multiple values, and vice versa. Fe XVI does follow the trend expected from the presence of a KG2 instrumental response. However, again we see different values of W for a single κ index, and vice versa.

We also examined the Fe XVI line profiles present in other, smaller solar flares. We looked for the presence of Gaussian Fe XVI profiles that would completely rule out an instrumental cause, but we found that the line profiles were difficult to analyze due to low intensity and high noise levels. We also obtained two sets of laboratory data when EIS was tested before launch. It was difficult to analyze the line shape with confidence due to the low EIS spectral pixel resolution, low line intensities, the presence of blends, and no available intensity error values.

References

Alexander, D. 1990, A&A, 236, L9
Antonucci, E., & Dodero, M. A. 1995, ApJ, 438, 480
Antonucci, E., Rosner, R., & Tsinganos, K. 1986, ApJ, 301, 975
Aschwanden, M. J. 2015, ApJL, 804, L20
Balanca, C., & Feautrier, N. 1998, A&A, 334, 1136
Battaglia, M., Kleint, L., Krucker, S., & Graham, D. 2015, ApJ, 813, 113
Bian, N. H., Emslie, A. G., Stackhouse, D. J., & Kontar, E. P. 2014, ApJ, 796, 142
Callen, J. D. 2006, Fundamental Processes in Plasmas (Madison, WI: Univ. Wisconsin Press)
Culhane, J. L., Harra, L. K., James, A. M., et al. 2007, SoPh, 243, 19
De Pontieu, B., Title, A. M., Lemen, J. R., et al. 2014, SoPh, 289, 2733
Dere, K. P., Landi, E., Mason, H. E., Monsignori Fossi, B. C., & Young, P. R. 1997, A&AS, 125, 149
Dere, K. P., & Mason, H. E. 1993, SoPh, 144, 217
Doschek, G. A., Feldman, U., Kreplin, R. W., & Cohen, L. 1980, ApJ, 239, 725
Doschek, G. A., Kreplin, R. W., & Feldman, U. 1979, ApJL, 233, L157
Francile, C., López, F. M., Cremades, H., et al. 2016, SoPh, 291, 3217
Gloeckler, G., & Geiss, J. 1998, SSRv, 86, 127
Heinzel, P., Kasparova, J., Varady, M., Karlicky, M., & Moravec, Z. 2016, arXiv:1602.00016
Heinzel, P., & Kleint, L. 2014, ApJL, 794, L23
Henoux, J. C., Chambe, G., Smith, D., et al. 1990, ApJS, 73, 303
Hnat, B., Chapman, S. C., Rowlands, G., Watkins, N. W., & Farrell, W. M. 2002, GeoRL, 29, 86
Holman, G. D. 1995, ApJ, 452, 451
Jeffrey, N. L. S., Fletcher, L., & Labrosse, N. 2016, A&A, 590, A99
Jones, A. W., Bland-Hawthorn, J., & Shopbell, P. L. 1995, in ASP Conf. Ser. 77, Astronomical Data Analysis Software and Systems IV, ed. R. A. Shaw, H. E. Payne, & J. J. E. Hayes (San Francisco, CA: ASP), 503
Judge, P. G., Kleint, L., Donea, A., Sainz Dalda, A., & Fletcher, L. 2014, ApJ, 796, 85
Judge, P. G., Kleint, L., & Sainz Dalda, A. 2015, ApJ, 814, 100
Kleint, L., Battaglia, M., Reardon, K., et al. 2015, ApJ, 806, 9
Kleint, L., Heinzel, P., Judge, P., & Krucker, S. 2016, ApJ, 816, 88
Klimchuk, J. A., Patsourakos, S., & Tripathi, D. 2016, SoPh, 291, 55
Kontar, E. P., Hannah, I. G., & Bian, N. H. 2011, ApJL, 730, L22
Kosugi, T., Matsuzaki, K., Sakao, T., et al. 2007, SoPh, 243, 3
Kowalski, A. F., Allred, J. C., Daw, A. N., Cauzzi, G., & Carlsson, M. 2016, arXiv:1609.07390
Krucker, S., Hurford, G. J., & Lin, R. P. 2003, ApJL, 595, L103
Landi, E., Young, P. R., Dere, K. P., Del Zanna, G., & Mason, H. E. 2013, ApJ, 763, 86
Lemen, J. R., Title, A. M., Akin, D. J., et al. 2012, SoPh, 275, 17
Li, Y., Ding, M. D., Qiu, J., & Cheng, J. X. 2015, ApJ, 811, 7
Lin, R. P., Dennis, B. R., Hurford, G. J., et al. 2002, SoPh, 210, 3
Liu, W., Heinzel, P., Kleint, L., & Kašparová, J. 2015, SoPh, 290, 3525
Livadiotis, G., & McComas, D. J. 2009, JGRA, 114, 11105
Matthews, S. A., Harra, L. K., Zharkov, S., & Green, L. M. 2015, ApJ, 812, 35
Milligan, R. O. 2011, ApJ, 740, 70
Milligan, R. O. 2015, SoPh, 290, 3399
Pesnell, W. D., Thompson, B. J., & Chamberlin, P. C. 2012, SoPh, 275, 3
Pierrard, V., & Lazar, M. 2010, SoPh, 267, 153
Pucci, F., Malara, F., Perri, S., et al. 2016, MNRAS, 459, 3395
Rubio da Costa, F., Kleint, L., Petrosian, V., Liu, W., & Allred, J. C. 2016, ApJ, 827, 38
Sigmar, D. J., & Joyce, G. 1971, NucFu, 11, 447
Simões, P. J. A., Hudson, H. S., & Fletcher, L. 2015, SoPh, 290, 3625
Sorriso-Valvo, L., Carbone, V., Veltri, P., Consolini, G., & Bruno, R. 1999, GeoRL, 26, 1801
Stix, T. H. 1972, PlPh, 14, 367
Vilmer, N., MacKinnon, A. L., & Hurford, G. J. 2011, SSRv, 159, 167
Young, P. R., Tian, H., & Jaeggli, S. 2015, ApJ, 799, 218